Nanoscale

REVIEW

View Article Online
View Journal

Cite this: DOI: 10.1039/d5nr05405b

Computational progress of designing single-atom alloy catalysts for methane activation

Chengyu Zhou and Qing Zhao *

Nonoxidative coupling of methane to value-added hydrocarbons remains a major challenge in catalysis due to inert C–H bonds in methane and rapid catalyst deactivation caused by coke contamination. Single-atom alloys (SAAs), atomically dispersing isolated metal atoms into a host metal surface, have emerged as promising catalysts for activating light alkanes. Here, we present a review of recent progress on designing SAA catalysts for the efficient and selective conversion of methane and other alkanes using computational modeling tools, including quantum mechanical simulations and machine learning models. First, we describe various studies applying first-principles simulations to discern reaction mechanisms, understand the role of isolated dopant atoms in reducing C–H activation barriers, and rationalize the synergy between the dopant and host in improving selectivity towards desired products. Next, we present how the rapid development of machine learning models enables the high-throughput screening of different dopants, hosts, and facets of SAA catalysts for methane transformation. We then extend the discussion from methane to the chemistry of activating other light alkanes, demonstrating that the dopant-host synergy promoting methane activation can also be applied to multi-carbon hydrocarbons. Finally, we provide some perspectives on the future outlook for the computational SAA catalyst design for methane activation. The goal of this review article is to present a computational perspective that systematically bridges first-principles mechanistic insights with data-driven workflows to enable the discovery of active, selective, and coke-resistant SAA catalysts for methane and light-alkane activation.

Received 22nd December 2025,
Accepted 21st March 2026

DOI: 10.1039/d5nr05405b

rsc.li/nanoscale

Department of Chemical Engineering, Northeastern University, Boston, MA 02115, USA. E-mail: q.zhao@northeastern.edu

Qing Zhao

Qing Zhao is an Assistant Professor of Chemical Engineering at Northeastern University. She received her PhD degree from the Massachusetts Institute of Technology in 2019 with Prof. Heather Kulik and completed a postdoc at Princeton with Prof. Emily Carter from 2018 to 2021, prior to joining Northeastern as a faculty member in January 2022. Her research focuses on developing and applying electronic structure theory to understand fundamental chemistry in heterogeneous catalysis and to design catalysts for energy and sustainability applications. She has received the NSF CAREER Award and the ACS Petroleum Research Fund Doctoral New Investigator Award.

1. Introduction

Methane, due to its substantial reserves in natural gas and shale formations, is an abundant carbon feedstock for chemical production.[1,2] However, its industrial valorization remains dominated by an indirect route, *i.e.*, steam methane reforming to generate syngas, followed by the Fischer–Tropsch synthesis.[3] Although established and scalable, this route requires enormous energy consumption and suffers from rapid catalyst deactivation caused by coke formation, leading to low thermodynamic efficiency and massive CO_2 emissions.[2,4–6] Two challenges of efficiently converting methane into value-added multi-carbon hydrocarbons, such as ethylene,[1,7] are that (1) the C–H bond in CH_4 is exceptionally strong with ~439 kJ mol^{-1}, demanding high temperatures over 700 °C,[8,9] and (2) partially dehydrogenated intermediates are strongly chemisorbed on catalyst surfaces, leading to catalyst deactivation.[10,11] The nonoxidative coupling of methane, bypassing syngas formation, is more environmentally and economically desirable.[12,13] However, this approach still faces the above two challenges.[14–18] Thus, a catalyst that can simultaneously activate C–H bonds and enable C–C coupling to avoid full dehydrogenation is promising for the efficient and selective conversion of methane to multi-carbon hydrocarbons.[7,19]

Single-atom alloys (SAAs), atomically dispersing active metal atoms into less active metal surfaces, have emerged as promising catalysts to overcome the above challenges in methane activation (Fig. 1).[20–35] The synergy between active dopants and host metal lowers the C–H activation barriers and simultaneously moderates the binding strength of carbonaceous adsorbates to promote selective C–C coupling.[19,25] SAA catalysts, such as Pt/Cu and Rh/Cu (*i.e.*, one Pt atom and one Rh atom doped into Cu surface, respectively), have experimentally shown remarkable alkane dehydrogenation performance.[28,29] These SAA catalysts are able to operate at much lower temperatures (<400 °C) than their counterpart host metals (>900 °C) while achieving high selectivity towards desired products (>90%) and enhanced resistance to coking.[27–29,36–40] However, the mechanistic understanding of SAAs across compositions, facets, and operating conditions is necessary towards designing more efficient SAAs.

Computational modeling plays a critical role in revealing the reaction mechanisms for generating critical hydrocarbons,[41–43] providing atomic-level understanding of catalyst reactivity, thereby accelerating catalyst discovery.[44–49] Density functional theory (DFT) calculations reveal important chemical insights through the predictions of adsorption energies and reaction mechanisms on well-defined active sites in SAA catalysts.[24,28,34,35,50–60] Combining free energy calculations with *ab initio* molecular dynamics (AIMD) simulations can capture temperature and entropic effects, ensuring thermodynamically consistent descriptions of reaction energies under experimentally relevant conditions.[53,61,62] Microkinetic modeling further incorporates experimental operating conditions and then translates elementary-step kinetics into macroscopic observables, connecting computational predictions with experimental observations in SAA catalyst design.[62–65] However, DFT simulations demand extensive computational resources for a large SAA chemical space, thereby limiting the scalability of DFT for SAA catalyst discovery.[66–69] Consequently, substantial efforts have been devoted to reducing the computational cost by developing simple yet reliable descriptors (*i.e.*, adsorption energies) and design principles (*i.e.*, Sabatier principle) derived from DFT calculations.[70–75] Building on the first-principles framework, machine learning (ML) provides a high-throughput screening strategy for accelerating SAA discovery.[63,64,76–80] Trained on carefully constructed DFT datasets, ML models can achieve near DFT-level accuracy across broad compositional and structural spaces, enabling efficient screening over various dopants, hosts, and facets, and provide interpretable insights into catalyst activity and selectivity.[77–81]

This review focuses on the computational progress of discovering SAA catalysts for direct methane activation, with an extension to the activation of other alkanes, including ethane and propane. We first provide first-principles insights into SAAs for the nonoxidative coupling of methane, including elucidating reaction mechanisms, developing effective descriptors, and performing microkinetic modeling. We then introduce ML models for SAA discovery, including dataset generation, model development, and result interpretation. We also extend the review to the activation of other alkanes, such as ethane and propane dehydrogenation, to understand the generalizability of SAAs in activating long-chain hydrocarbons. We close by summarizing key chemical insights and proposing strategies and principles for the future design of reactive, selective, and stable SAA catalysts for alkane activation.

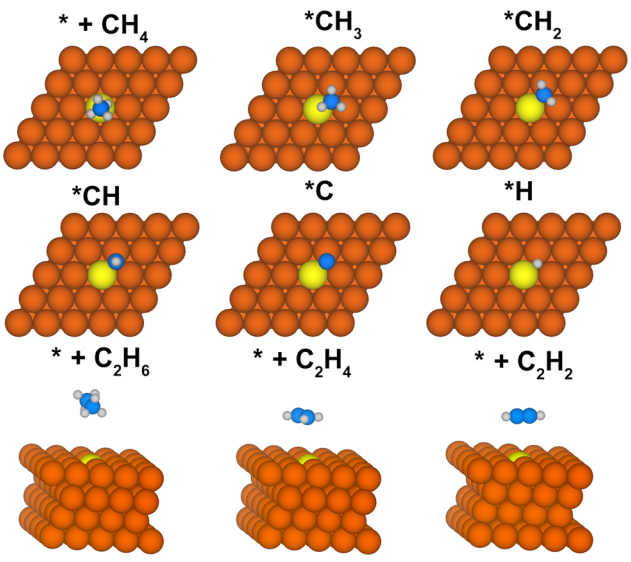

Fig. 1 Representative structures of methane activation and C–C coupling mechanisms leading to C_2 products on SAAs. Atoms are colored as follows: orange for the host metal, yellow for the dopant metal, blue for carbon, and light gray for hydrogen.

2. First-principles studies on SAAs for methane activation

First-principles methods, particularly DFT, enable the prediction of reaction energetics and provide mechanistic insights into how isolated dopants reduce C–H activation barriers. These studies identify key catalytic descriptors underlying dopant–host synergy, including intermediate adsorption energies and transition-state geometries. In addition, first-principles calculations generate the datasets used to train the ML models discussed in the subsequent section on ML studies. Therefore, establishing a first-principles understanding of the electronic properties and reaction mechanisms governing methane activation is a critical prerequisite for implementing data-driven ML approaches.

Kokalj *et al.*[50] performed one of the earliest DFT studies with the Perdew–Burke–Ernzerhof (PBE)[82] exchange–correlation (XC) functional on methane dehydrogenation over Rh/Cu(111) SAA (the notation A/B denotes a single atom (A) dispersed in the surface layer of host B). They found that by dispersing a highly active Rh atom in the surface layer of a less reactive Cu(111) surface, the barrier for the first C–H bond breaking (*i.e.*, $*CH_4 \rightarrow *CH_3 + *H$, * denotes adsorbed species) could be largely reduced from 1.7 eV to 0.7 eV, which was

almost identical to 0.69 eV on a pure Rh(111). Interestingly, the subsequent dehydrogenation step, *i.e.*, $*CH_3 \rightarrow *CH_2 + *H$, is kinetically more difficult than the first step due to the blockage of the active sites around $*CH_3$, suggesting that the Rh/Cu(111) SAA catalyst can effectively suppress further dehydrogenation and thereby mitigate coke formation. This work established a key foundation in SAA catalysis, in which the synergy between active dopants and less active hosts can decouple sequential dehydrogenation steps, enhancing both activity and selectivity. Zhang *et al.*[52] further investigated the role of Rh dopants in enhancing the catalytic reactivity of Cu(111) surfaces for methane activation using DFT calculations with the Perdew-Wang 91 (PW91) XC functional.[83] This work compares the reaction barriers of methane dehydrogenation on a pure Cu(111), a single Rh atom adsorbed on Cu(111), and a Rh/Cu(111) SAA. An embedded Rh atom is found to substantially lower the barrier for the first C–H bond cleavage from 2.16 eV on pure Cu(111) to 0.87 eV on Rh/Cu(111), indicating the great potential of Rh as a dopant to facilitate methane dehydrogenation. The barriers for the second, third, and fourth dehydrogenation steps are similarly reduced, from 1.72 to 1.17 eV, from 1.30 to 0.97 eV, and from 2.30 to 1.50 eV, respectively. Interestingly, a single Rh adatom on Cu(111) exhibits comparable activity in lowering the first and second C–H activation barriers. However, the barrier for the third dehydrogenation step remains higher on the Rh adatom surface (1.30 eV) than on Rh/Cu(111) SAA (0.97 eV). For the fourth dehydrogenation step, the barrier is lower on the Rh adatom surface (1.09 eV) than on Rh/Cu(111) SAA (1.50 eV), indicating the uniqueness of SAA in suppressing coke formation. The reaction energies and activation barriers of each methane dehydrogenation step on various SAAs are summarized in Table 1, grouped by host metals, including Ag, Au, Cu, Ni, Pt, and Rh.

A screening work was later conducted using DFT with the optB86b-vdW XC functional[84–87] by Darby *et al.*[24] to examine methane adsorption and the first C–H bond cleavage of methane across 12 SAA catalysts, comprising active dopants of Ni, Pd, Pt, and Rh embedded in less reactive host metals of Cu(111), Ag(111), and Au(111). They show that the dopant sites are the dominant active sites, *i.e.*, CH_4 activation occurring at the dopant top site, where the transition state structure is stabilized by the active dopant. Subsequently, the dissociated *H migrates to a dopant–host interfacial hollow site, while $*CH_3$ remains on the dopant top site. The reactive dopants result in surmountable barriers of the first C–H bond breaking step, including 0.82 eV for both Ni/Ag(111) and Ni/Cu(111); 0.94, 0.85, and 0.92 eV for Pt/Ag(111), Pt/Au(111), Pt/Cu(111), respectively; and particularly low barriers of 0.55, 0.61, and 0.64 eV for Rh/Ag(111), Rh/Au(111), Rh/Cu(111), respectively. The isolated dopants remarkably lower the reaction barriers of C–H bond cleavage compared to the pure metal hosts (2.11, 1.78, and 1.48 eV for Ag, Au, and Cu, respectively), achieving barriers close to their corresponding bulk materials (Ni(111): 0.75 eV; Pd(111): 0.68 eV; Pt(111): 0.58 eV; Rh(111): 0.56 eV). In addition, Fig. 2 demonstrates that the Brønsted–Evans–Polanyi (BEP) relationship remains valid across the 12 SAAs but shifts towards a lower reaction barrier compared to pure metals due to the dopant–host synergy. In general, SAAs tune the binding energies of adsorbates to achieve intermediate strengths between those on host metals and dopant metals, to both enhance reactivity and reduce coke formation.

In addition to the initial methane dehydrogenation step, Jiang *et al.*[54] employed DFT with the PW91 XC functional to study the complete methane dehydrogenation pathway on pure Cu(111) and Cu(111)-based SAAs with Pd, Pt, Rh, and Ni single dopants (Table 1). All studied SAAs exhibit enhanced activity compared to pure Cu(111) with significantly decreased reaction barriers for all C–H bond cleavages of CH_4. In addition, they found that the activity trend followed Rh > Ni > Pt > Pd in terms of both kinetic and thermodynamic favorability, consistent with the findings of Darby *et al.*[24] Particularly, Rh/Cu(111) SAA exhibits the lowest reaction energies and activation barriers for all dehydrogenation steps, making it the optimal SAA catalyst for methane activation. Furthermore, the last dehydrogenation step of $*CH \rightarrow *C + *H$ was identified as the universal rate-limiting step across all studied SAAs, consistent with previous studies.[52] This work shows that all four active dopants can improve the reactivity of Cu surface for methane activation, with Rh/Cu(111) SAA as the most promising one.

Hannagan *et al.*[29] studied the same dopants of Ni, Pd, Pt, and Rh, but extended the host metals from Cu(111) to Ag(111) and Au(111) for methane activation using DFT with optB86b-vdW XC functional. They also found that the Rh-doped SAAs exhibited the lowest C–H activation barriers, consistent with previous studies showing the great potential of Rh dopants in activating methane.[24,52,54] Among different metal hosts, Rh/Cu(111) exhibits both lower C–H activation barriers and higher thermodynamic stability (Fig. 3A). Electronic structure analysis reveals that methane adsorbs closer to the Rh dopant site on Rh/Cu(111) than to the Cu site on pure Cu(111) and exhibits stronger charge redistribution from C–H bond to H···Rh internuclear region than on pure Cu(111), indicating the activation of methane upon adsorption on Rh/Cu(111) SAA (Fig. 3B). Reaction energy profiles indicate that further dehydrogenation steps leading to coke formation occur more easily on pure Pt(111) than on pure Cu(111) and Rh/Cu(111) SAA surfaces, whereas the subsequent dehydrogenation steps are unfavored on Rh/Cu(111) due to the predicted large reaction energies (Fig. 3C). Akça[56] performed a detailed study of methane dehydrogenation on Pd/Cu(111) SAA using DFT with PBE XC functional, confirming that the incorporation of Pd dopants reduced the barriers of the initial C–H bond cleavage by 0.48 eV compared to a pure Cu(111) surface while showing negligible effects on the second and third steps.

Marcinkowski *et al.*[28] combined DFT with optB86b-vdW XC functional, surface science experiments, and microkinetic modeling to explore the catalytic reactivity of Pt/Cu(111) SAA for C–H activation and demonstrated that Pt/Cu SAA could efficiently activate C–H bonds while resisting coke formation. Isolated Pt atoms dispersed on a Cu(111) surface serve as highly active sites that lower the first C–H bond activation

Table 1 Reaction energies (ΔE_{rxn}) and activation barriers (E_a) in eV of the methane dehydrogenation steps on various SAA surfaces, along with the applied DFT XC functionals and references, reported in the literature. Table highlights three mechanistic trends emerging from the reported DFT studies: (1) introducing an isolated dopant substantially lowers the barrier of the initial C–H activation compared with the pure host metal, thereby making methane activation kinetically accessible, (2) among the widely studied SAAs featuring Ni, Pd, Pt, and Rh dopants on Ag, Au, and Cu hosts, Rh-doped SAAs consistently exhibit the lowest barrier for the first C–H cleavage, and (3) when full dehydrogenation mechanisms are reported (*e.g.*, for Cu- and Ni-host cases), the last step (*CH → *C + *H) is rate-limiting, highlighting that high activity for the first dehydrogenation step does not necessarily imply facile deep dehydrogenation

	$CH_4 \rightarrow *CH_3 + *H$		$CH_3 \rightarrow *CH_2 + *H$		$CH_2 \rightarrow *CH + *H$		$CH \rightarrow *C + *H$			
SAAs	E_a	ΔE_{rxn}	E_a	ΔE_{rxn}	E_a	ΔE_{rxn}	E_a	ΔE_{rxn}	XC functional	Ref.
Ag host										
Ni/Ag(111)	0.82	0.69	—	—	—	—	—	—	optB86b-vdW	24
Pd/Ag(111)	1.21	1.02	—	—	—	—	—	—	optB86b-vdW	24
Pt/Ag(111)	0.94	0.59	—	—	—	—	—	—	optB86b-vdW	24
Rh/Ag(111)	0.55	0.35	—	—	—	—	—	—	optB86b-vdW	24
Au host										
Ni/Au(111)	0.94	0.94	—	—	—	—	—	—	optB86b-vdW	24
Pd/Au(111)	1.18	1.02	—	—	—	—	—	—	optB86b-vdW	24
Pt/Au(111)	0.85	0.56	—	—	—	—	—	—	optB86b-vdW	24
Rh/Au(111)	0.61	0.47	—	—	—	—	—	—	optB86b-vdW	24
Cu host										
Pure Cu(111)	1.30	0.50	1.16	0.61	0.85	0.34	1.71	1.14	optB86b-vdW	29
Pure Cu(111)	2.16	0.85	1.72	0.86	1.30	0.64	2.30	1.42	PW91	52
Pure Cu(111)	1.77	1.07	1.62	1.12	1.13	0.88	2.06	1.82	PW91	54
Pure Cu(111)	1.32	—	1.24	—	0.87	—	2.03	—	PBE	56
Cr/Cu(111)	0.64	0.22	0.76	0.24	0.24	−0.11	1.26	0.76	PBE	35
Ir/Cu(111)	0.25	−0.01	0.59	0.32	0.42	−0.09	1.13	0.46	PBE	35
Ni/Cu(111)	0.82	0.56	—	—	—	—	—	—	optB86b-vdW	24
Ni/Cu(111)	0.77	0.43	0.75	0.50	0.54	0.35	1.33	0.84	PBE	35
Ni/Cu(111)	0.99	0.41	0.71	0.46	0.59	0.28	1.51	1.20	PW91	54
Pd/Cu(111)	1.19	0.80	—	—	—	—	—	—	optB86b-vdW	24
Pd/Cu(111)	1.27	0.67	1.26	0.91	1.07	0.71	1.92	1.42	PW91	54
Pd/Cu(111)	0.84	—	1.11	—	0.80	—	1.98	—	PBE	56
Pt/Cu(111)	0.92	0.53	—	—	—	—	—	—	optB86b-vdW	24
Pt/Cu(111)	0.86	0.30	0.96	0.62	0.75	0.31	1.49	0.90	optB86b-vdW	29
Pt/Cu(111)	1.11	0.40	1.11	0.73	1.07	0.65	1.86	1.39	PW91	54
Rh/Cu(111)	0.64	0.34	—	—	—	—	—	—	optB86b-vdW	24
Rh/Cu(111)	0.57	0.38	0.54	0.42	0.38	0.13	1.20	0.69	optB86b-vdW	29
Rh/Cu(111)	0.35	0.08	0.71	0.38	0.51	0.20	1.22	0.51	PBE	35
Rh/Cu(111)	0.70	0.36	0.84	0.59	—	—	—	—	PBE	50
Rh/Cu(111)	0.87	0.41	1.17	0.55	0.97	0.23	1.50	0.73	PW91	52
Rh/Cu(111)	0.83	0.39	0.76	0.41	0.45	0.01	1.48	0.97	PW91	54
W/Cu(100)	0.70	−0.25	0.97	0.04	0.98	−0.43	1.25	0.27	PW91	55
Ni host										
Pure Ni(111)	0.92	0.02	—	—	—	—	1.28	0.46	PBE	51
Pure Ni(111)	0.90	−0.53	0.71	0.03	0.25	−0.50	1.22	0.36	PBE	60
Pure Ni(100)	0.83	0.16	—	—	—	—	0.52	−0.25	PBE	51
Pure Ni(211)	0.53	−0.32	—	—	—	—	0.51	−0.22	PBE	51
Al/Ni(111)	1.65	−0.35	0.70	0.33	0.90	−0.78	1.17	0.29	PBE	60
Cu/Ni(111)	1.49	−0.18	1.19	0.09	0.60	−0.33	1.82	−0.12	PBE	60
Fe/Ni(111)	1.02	−0.36	0.94	−0.01	0.46	−0.33	1.26	0.49	PBE	60
Pd/Ni(111)	1.06	0.38	—	—	—	—	1.28	0.59	PBE	51
Pd/Ni(111)	1.08	−0.13	0.91	0.10	0.69	−0.54	1.59	0.47	PBE	60
Pd/Ni(100)	0.94	0.27	—	—	—	—	0.74	−0.03	PBE	51
Pd/Ni(211)	0.62	0.06	—	—	—	—	0.66	−0.09	PBE	51
Pt/Ni(111)	0.89	−0.07	0.63	−0.21	0.82	−0.40	1.43	0.52	PBE	60
Zn/Ni(111)	0.95	0.02	1.86	0.07	0.57	−0.89	1.16	0.28	PBE	60
Pt and Rh hosts										
Pure Pt(111)	0.51	−0.27	0.58	−0.06	0.10	−0.71	1.16	0.41	optB86b-vdW	29
Pure Rh(111)	0.46	−0.30	0.31	−0.28	0.04	−0.56	1.01	0.32	optB86b-vdW	29
Pure Rh(111)	0.69	0.22	0.42	−0.10	—	—	—	—	PBE	50

barrier from 1.48 eV on a pure Cu(111) surface to 0.92 eV. In general, reaction barriers for the full methane dehydrogenation steps on Pt/Cu(111) SAA are lower than those on a pure Cu(111), but higher than those on a pure Pt(111), enabling methane dehydrogenation at lower temperatures than those for Cu(111) and simultaneously suppressing coke formation (Fig. 4). Experimentally, Pt/Cu SAA is stable and active over a long operation time, while the monometallic Pt surface rapidly deactivates due to coke deposition. This work highlights that the SAA catalyst outperforms its pure metal components.

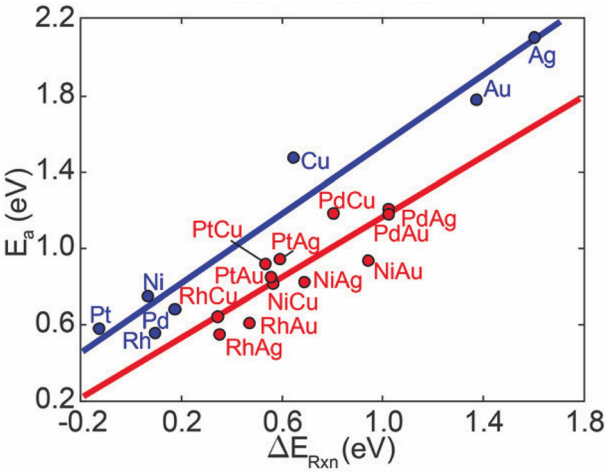

Fig. 2 BEP relationship for the first C–H bond cleavage in methane on pure metal surfaces (blue) and SAA surfaces (red). The activation energy (E_a) is plotted against the reaction energy (ΔE_{rxn}) with linear fitting lines shown for each surface type. Reproduced from ref. 24, with permission from the American Chemical Society, copyright 2018.

Afterwards, Gerrits *et al.*[53] combined DFT with AIMD to investigate the initial C–H bond activation of CHD_3 on Cu surfaces and Cu-based SAAs. Their findings are consistent with those of a previous work showing that the C–H activation barrier is dramatically reduced on Pt/Cu(111) and the C–H activation only occurs near the Pt top site.[28]

Zhao *et al.*[51] extended the SAA studies from Cu to Ni metal host and employed DFT with the PBE[82] XC functional to study the thermodynamic stability of Pd/Ni SAAs and how Pd doping influences methane dehydrogenation on Ni(111), Ni(100), and Ni(211) facets. They found that SAA with isolated Pd atoms embedded on the Ni surface layer had the most negative formation energy compared with Pd atoms immersed in the Ni bulk or adsorbed on the Ni surface, indicating the formation of Pd/Ni SAAs. Interestingly, they predicted that although Pd dopants reduced the binding strength of most intermediates, including *CH_3, *CH, *C, and *H, they increased the activation barriers of both CH_4 and *CH dehydrogenation. This is divergent from Pd/Cu SAAs, likely due to the higher reactivity of Ni than that of Cu for methane activation.[29,54,56] Among the Pd/Ni SAAs, CH_4 dehydrogenation is the most favored on the stepped Pd/Ni(211) surface, followed by the Pd/Ni(100) surface and then the close-packed Pd/Ni(111) surface (Table 1). In a different study by Dong *et al.*,[60] focusing on Ni(111)-based SAAs with dopants spanning Cu, Fe, Pt, Pd, Zn and Al, they found that Al and Zn dopants could reduce the barrier of the final *CH → *C + *H step, whereas Pt dopant lowered the barriers of CH_4 → *CH_3 + *H and *CH_3 → *CH_2 + *H. Additionally, *C adsorbates tend to aggregate and form graphitic layers, thereby destabilizing surface intermediates and increasing activation barriers for all dehydrogenation steps. This explains the mechanisms of coke formation and how it suppresses further methane activation and deactivates catalyst surfaces.

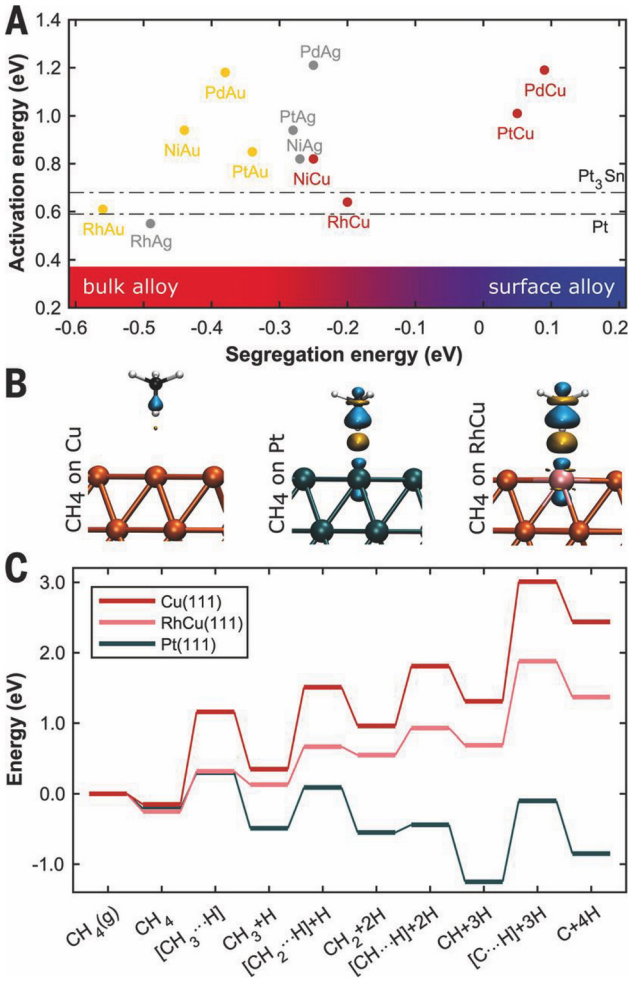

Fig. 3 (A) Relationship between the activation barriers of the first C–H bond cleavage on various SAAs and the SAA segregation energies. Activation barriers on Pt(111) and Pt_3Sn are shown as dotted-dashed lines. (B) Charge density difference of CH_4 adsorbed on Cu(111), Pt(111), and Rh/Cu(111) SAA surfaces. Cu, Pt, and Rh atoms are colored as orange, teal, and pink, respectively. Cyan and yellow contours indicate regions of electron depletion and accumulation with an isosurface value of ±0.01 e $Å^{-3}$. (C) Energy profiles of full methane dehydrogenation steps on pure Cu(111) (red), Rh/Cu(111) (pink), and pure Pt(111) (green) surfaces. Reproduced from ref. 29, with permission from AAAS, copyright 2021.

Other recent DFT studies explored additional SAA dopants. For example, Khettal *et al.*[55] focused on the performance of W/Cu SAAs and found that W/Cu(100) exhibited surmountable reaction energies and activation barriers for CH_4 dehydrogenation, indicating that W may serve as an effective dopant to enhance methane activation on Cu surfaces. Ren *et al.*[57] used DFT with the PBE XC functional to examine methane activation on SAAs, with Ir atoms atomically dispersed on several metal hosts, including Cu, Ag, Pd, Pt, Ni, and Rh, with three exposed facets, *i.e.*, (100), (110), and (111). The incorporation of Ir dopants into host metal surfaces effectively reduces the reaction barriers of the first C–H bond cleavage step by approximately 0.3 to 0.4 eV compared with the corresponding

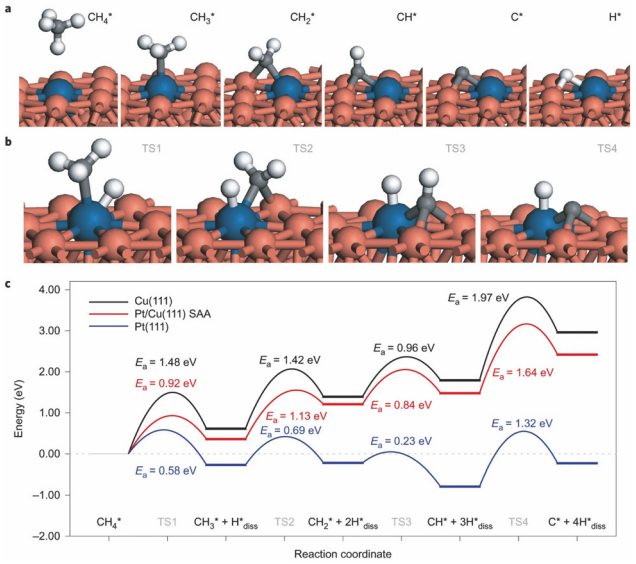

Fig. 4 Methane dehydrogenation on pure Cu(111), Pt/Cu(111) SAA, and pure Pt(111) predicted by DFT. (a) Optimized geometries of the most stable methane dehydrogenation intermediates on Pt/Cu(111). (b) Transition state structures of successive C–H bond cleavages of methane dehydrogenation on Pt/Cu(111). (c) Energy profiles of full methane dehydrogenation on Cu(111) (black), Pt/Cu(111) SAA (red), and Pt(111) (blue). Reproduced from ref. 28, with permission from Springer Nature, copyright 2018.

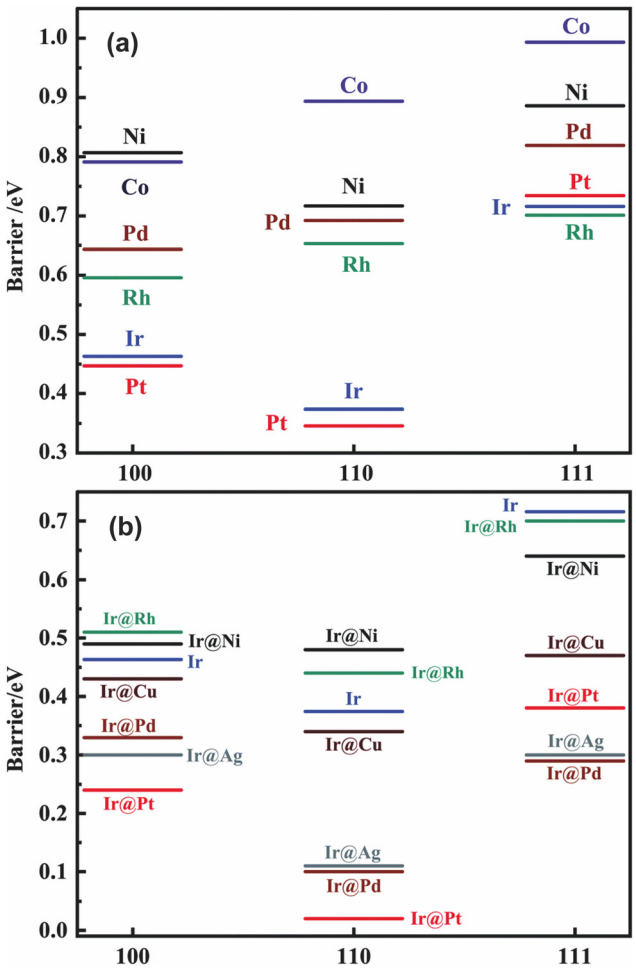

Fig. 5 Activation barriers of the first C–H bond breaking of methane on (a) pure metal surfaces and (b) SAA surfaces with Ir dopants across the (100), (110), and (111) facets. Reproduced from ref. 57, with permission from the Royal Society of Chemistry, copyright 2021.

pure host metal surfaces (Fig. 5). Surprisingly, Ir dopants not only activate less reactive host metals, such as Cu and Ag, but also improve the activity of more reactive metals, including Pd, Pt, and Ni, as revealed from their relatively low C–H activation barriers. The enhanced reactivity originates from the d-states of the Ir dopant, which promote electron transfer between the surface and the C–H bond, thereby stabilizing transition states and lowering the activation energies. Among all examined SAAs, Ir/Pt(110) has the highest catalytic activity, with an activation barrier that is close to 0 eV, highlighting that SAAs with Ir dopants are promising catalysts for low-temperature methane activation. However, this study only focused on the first C–H bond breaking, overlooking further dehydrogenation steps that might lead to coke formation.[28]

Zhou *et al.*[59] explored 12 SAAs for methane activation using DFT with PBE XC functional, including Ir, Ni, Pt and Rh dopants on Ag(111), Au(111), and Cu(111) metal hosts. Similarly, their results showed that SAAs with Ir dopants exhibit the highest activity for the first C–H bond cleavage compared with other dopants, arising from the strong interaction between the cleaved C–H bond and d-orbitals of Ir dopants, consistent with the above work.[57] Another work by Zhou *et al.*[58] screened a relatively large SAA chemical space of 12 metal dopants on 4 metal hosts, including Cu(111), Cu(100), Ag(111), and Ag(100), for the first C–H activation of methane using DFT with PBE XC functional. They found that even though the reaction energies and activation barriers generally follow the BEP relationship, relatively large mean absolute errors (MAE) of around 0.2 eV were observed (Fig. 6). Instead, they proposed a new descriptor that incorporated the adsorption energies of $*CH_3$ and *H intermediates to correlate with the C–H activation barriers across all studied SAAs (Fig. 7), enabling the accurate prediction of methane activation barriers on unexplored SAA surfaces.

Beyond methane dehydrogenation, the nonoxidative coupling of methane towards generating multi-carbon hydrocarbons represents a more industrially relevant and economically beneficial reaction.[34,35] Kothakonda *et al.*[34] performed a systematic screening of 27 Cu(111)-based SAAs with all possible 3d–5d transition metals for the nonoxidative coupling of methane to C_2 products, including ethane and ethylene, using DFT with PBE XC functional. They started by calculating the aggregation and segregation energies of all dopant–host combinations to assess the thermodynamic stabilities of SAAs and identified 16 stable SAAs for subsequent reactivity studies, including full dehydrogenation steps and possible C–C coupling steps to ethane and ethylene (Fig. 8). Among them, further

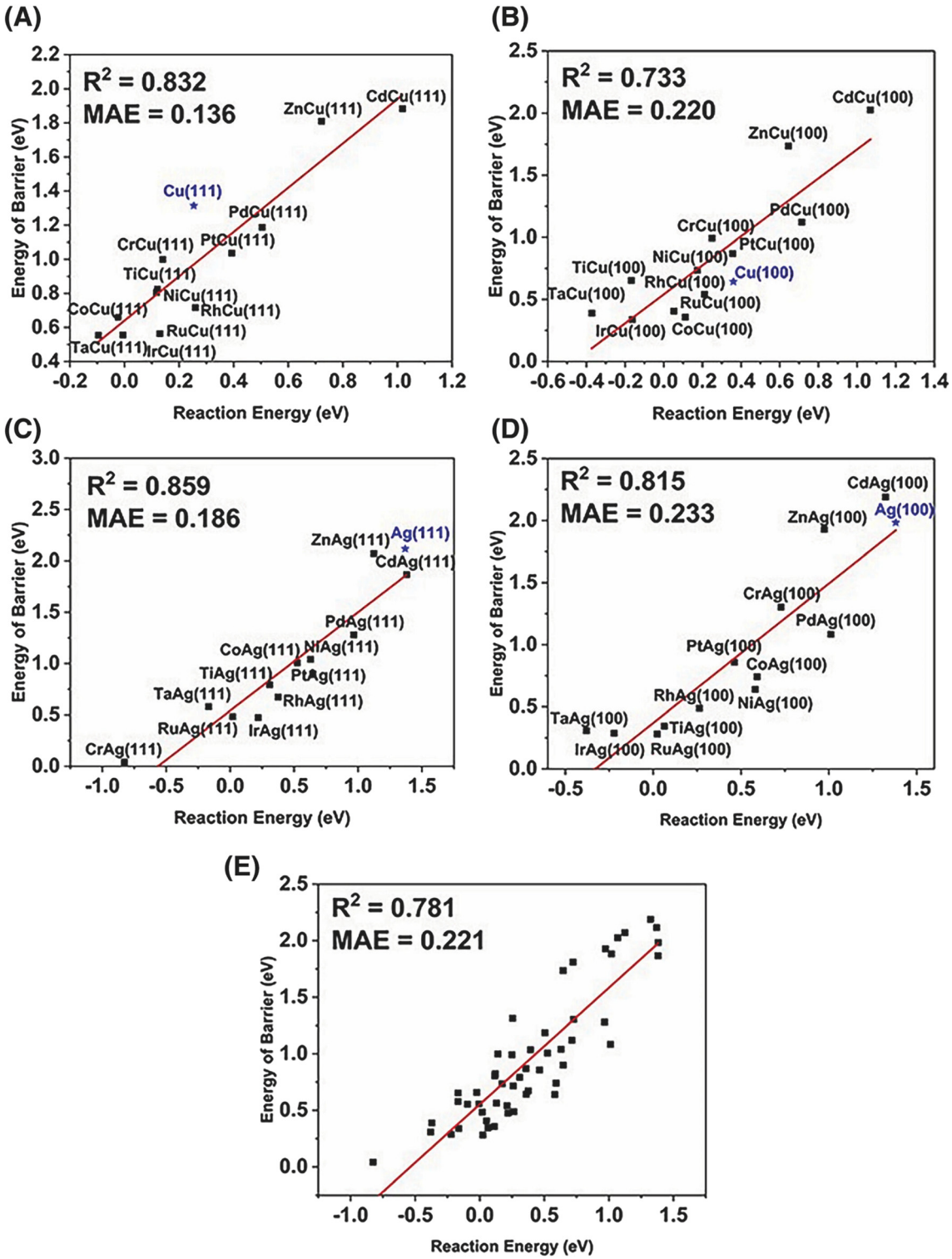

Fig. 6 BEP relationship of the first C–H bond activation of methane on SAAs with (A) Cu(111), (B) Cu(100), (C) Ag(111), (D) Ag(100), and (E) all metal hosts. Reproduced from ref. 58, with permission from John Wiley and Sons, copyright 2023.

selectivity analyses indicated that Ni/Cu(111), Rh/Cu(111), and Cr/Cu(111) SAAs exhibited both high activity and selectivity towards C_2 products based on thermodynamic favorability. To provide a more complete picture, they further performed kinetic calculations of the nonoxidative coupling of methane to both ethane and ethylene on these three SAA candidates and concluded that Ni/Cu(111) was a highly active and selective SAA for direct methane conversion to ethylene (Fig. 8).

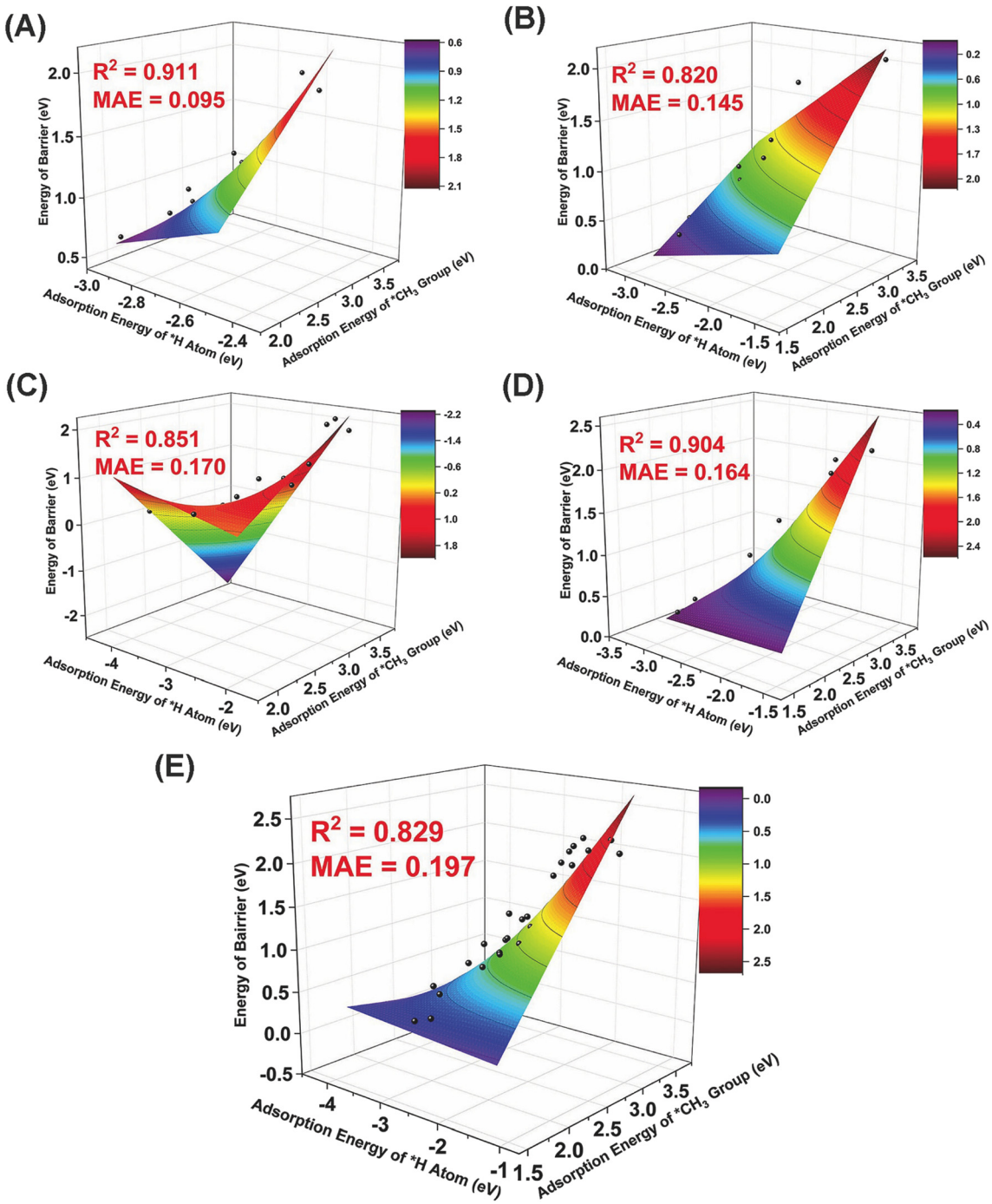

Fig. 7 Relationship between a binary descriptor incorporating the adsorption energies of $*CH_3$ and *H and the reaction barriers of the first C–H activation of methane on SAAs with (A) Cu(111), (B) Cu(100), (C) Ag(111), (D) Ag(100), and (E) all metal hosts. Reproduced from ref. 58, with permission from John Wiley and Sons, copyright 2023.

Extending the work of Kothakonda *et al.*,[34] Zhou *et al.*[35] systematically computed the reaction barriers of all steps of the nonoxidative coupling of methane, including full dehydrogenation and two C–C coupling steps to ethane and ethylene, on ten Cu(111)-based SAAs, including Sc, Cr, Mn, Ni, Y, Zr, Rh, Hf, Ir, and Pt dopants, which showed reaction energies of less than 0.5 eV for the first C–H bond activation. A strong correlation between SAA activity and selectivity toward ethylene formation was observed, indicating that the synergy between dopant and host could simultaneously reduce C–H activation barriers and promote selective C–C coupling (Fig. 9). Interestingly, ethylene formation is kinetically favored over ethane formation across all studied SAAs (Fig. 9). In addition, $*C_2H_4$ adsorption energy was identified as an effective descrip-

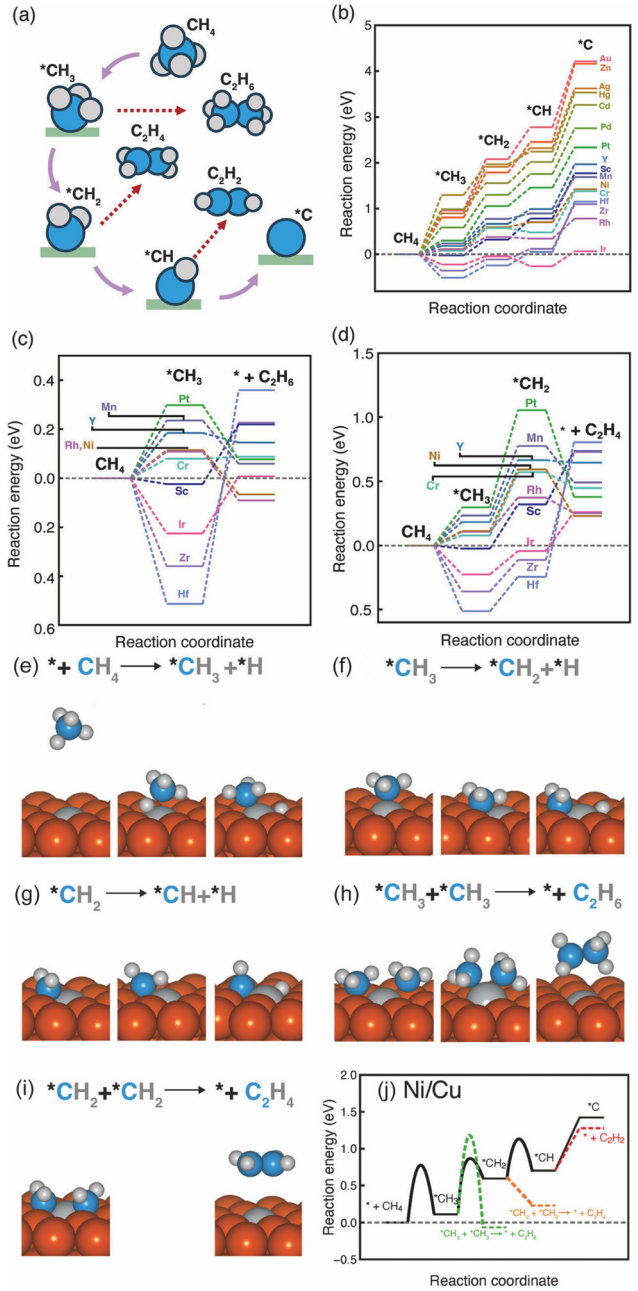

Fig. 8 (a) Schematic of methane dehydrogenation to *C and C–C coupling steps, forming ethane, ethylene, and acetylene. Atoms are colored blue for carbon and gray for hydrogen. (b) Energy landscapes for full methane dehydrogenation to *C on 16 stable SAAs. Energy landscapes for direct methane conversion to (c) ethane and (d) ethylene on 10 stable SAAs with the reaction energies of the first dehydrogenation step below 0.5 eV. SAAs are labeled using the corresponding dopant element. Structures of the initial, transition, and final states for (e–g) methane dehydrogenation and (h, i) C–C coupling to form C_2 products on Ni/Cu SAA. Energy landscapes for the full methane dehydrogenation to *C and C–C coupling to form C_2 products on (j) Ni/Cu SAA. Reproduced from ref. 34, with permission from the American Chemical Society, copyright 2025.

tor that correlates with SAA activity for direct methane conversion to ethylene (Fig. 9). Among all candidates, Ir/Cu(111) SAA emerges as the most kinetically favorable catalyst for methane to ethylene conversion.

The wide range of activation barriers reported for the same SAA, as shown in Table 1, underscores the sensitivity of predicted methane activation energetics to the choice of DFT XC functionals. Early studies primarily employed standard generalized gradient approximation (GGA) functionals, such as PBE[82] and PW91,[83] which are generally suitable for describing metallic bonding but do not explicitly account for long-range dispersion interactions. This limitation can be important because methane adsorption is weak, and both the physisorbed initial state and the stretched C–H transition state may be stabilized when van der Waals (vdW) interactions are included. Dispersion-inclusive functionals, such as optB86b-vdW,[84–87] can capture vdW interactions more accurately. However, they may overestimate adsorption energies for strongly chemisorbed intermediates, and thus, they often yield activation barriers that differ from those obtained with standard GGAs.[88,89] For example, for Rh/Cu(111) SAA, the reported barrier for the first C–H cleavage ranges from 0.35 eV (PBE) to 0.87 eV (PW91), while an optB86b-vdW study reports an intermediate value of 0.57 eV for the same step. Similar variations are observed for a pure host metal, Cu(111), showing a first-step barrier of 2.16 eV in a PW91 study, as compared with 1.30 eV obtained using optB86b-vdW. Importantly, despite these quantitative variations in activation barriers, the qualitative design trends for SAAs remain consistent across different functionals. Reactive dopants, such as Rh and Ni, substantially lower the first C–H activation barrier relative to the host metal regardless of functional choices, highlighting the robustness of DFT as a tool for studying SAA reactivity.

3. Machine learning studies on SAAs for methane activation

Over the past decade, ML has attracted great attention among the computational catalysis community for its capability in accelerating catalyst design through high-throughput screening.[90–102] ML serves as a fast and accurate alternative to first-principles modeling by learning structure–composition–property relationships from DFT-constructed datasets and then inferring physical correlations and predicting catalytic behavior across vast chemical spaces, thereby providing a scalable route to explore large compositional and structural domains.[103–110] However, it is challenging to accurately identify convoluted relationships between bulk/surface structures and catalytic performances, emphasizing the need for interpretable descriptors that govern activity and selectivity. This section summarizes recent ML-based efforts to discover efficient catalysts for methane activation and unearth key descriptors and design principles.

Toyao *et al.*[76] developed regression models to predict the DFT-computed adsorption energies of methane dehydrogena-

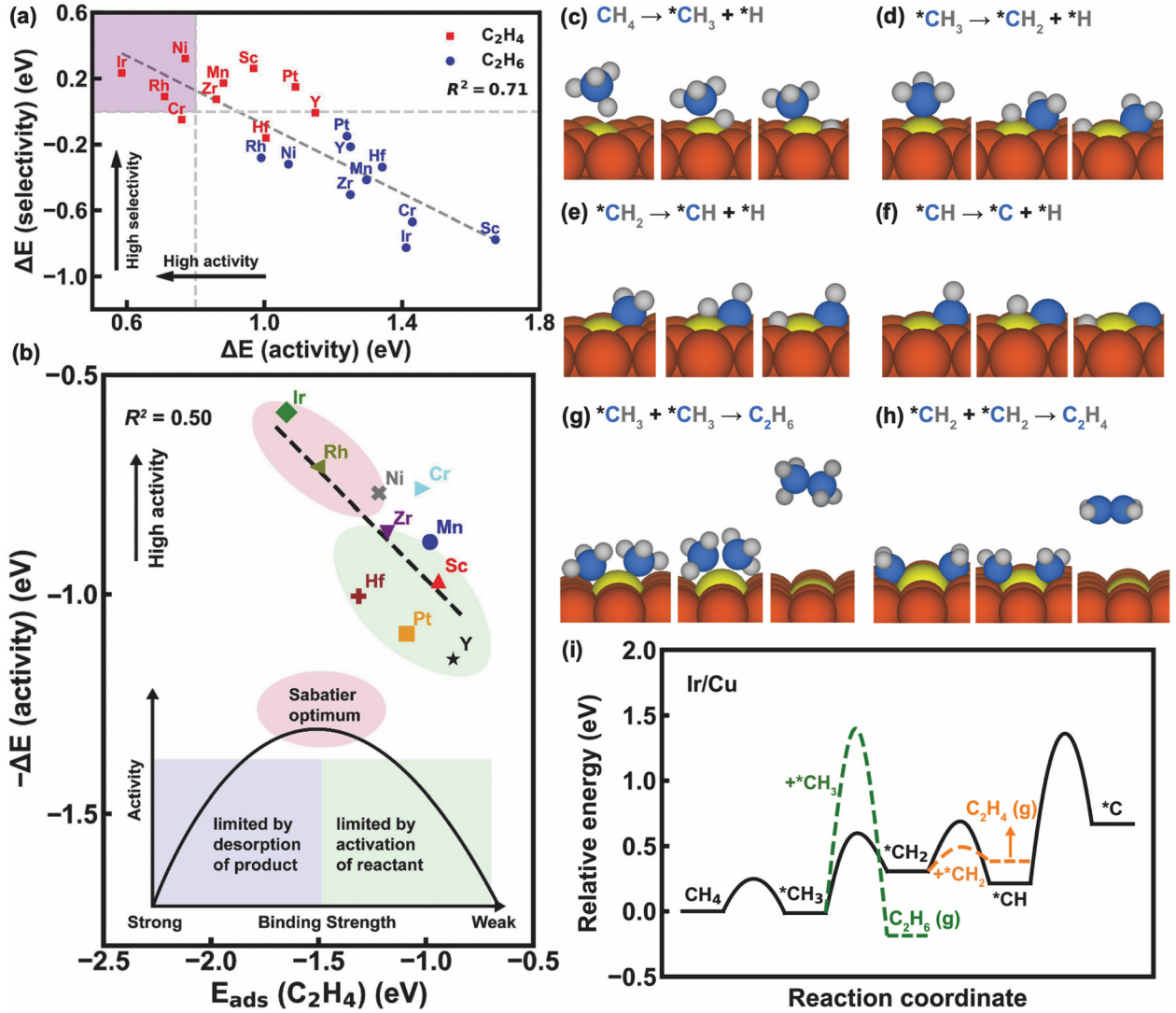

Fig. 9 (a) Correlation between the activity and selectivity of ten Cu-based SAA catalysts for direct methane conversion to ethane (blue circles) and ethylene (red squares). The dashed gray line shows the linear fit with R^2 inset. The vertical and horizontal gray dashed lines indicate an activity of 0.8 eV and a selectivity of 0.0 eV, respectively. The upper-left purple region indicates SAAs with both high activity and high selectivity. (b) Correlation between the negative reaction barrier of the rate-limiting step and the ethylene adsorption energy for ten SAAs. The dashed black line denotes the linear fit with R^2 inset. The inset schematic illustrates the Sabatier principle, with the blue region representing desorption-limited reactivity and the green region representing activation-limited reactivity. Structures of the initial, transition, and final states for (c–f) methane dehydrogenation steps and (g–h) C–C coupling steps to form C_2 products on Ir/Cu SAA. (i) Energy profile of methane dehydrogenation to *C (black solid line), $*CH_3$ coupling to ethane (green dashed line), and $*CH_2$ coupling to ethylene (orange dashed line) on Ir/Cu SAA. Reproduced from ref. 35, with permission from Elsevier, copyright 2025.

tion intermediates, $*CH_x$ species (x = 3, 2, 1, and 0) and *H, on Cu(111)-based SAAs using 12 descriptors of the physical properties of the dopant.[111–114] DFT datasets contain 46 data points, *i.e.*, 46 SAA surfaces, for each adsorbate. They systematically compared four regression models and found that the extra tree regression (ETR) model showed the best performance in predicting the adsorption energies, with the average root mean squared errors (RMSEs) below 0.3 eV. Feature importance analysis revealed that the periodic group, surface energies, and melting points of the dopant elements were the most important descriptors to predict the adsorption energies. Other works show that the periodic group and surface energies are common descriptors for catalytic performances.[115,116] This ML model only requires small DFT datasets and negligible computational cost, and thus, it could be used to rapidly screen a large chemical space of SAA catalysts for methane activation. Later, Saxena *et al.*[63] employed a similar framework and selected the gradient boosting regression (GBR) model to predict atomic *C and *O binding energies on Cu-based SAAs, using the same set of descriptors,[113,114,117] achieving accuracies of RMSE below 0.4 eV. Similarly, feature importance analysis identifies surface energies and periodic groups of

dopants as dominant descriptors, which is consistent with the above work by Toyao *et al.*[76]

Han *et al.*[78] integrated first-principles calculations with the compressed-sensing data-analytic method, namely the sure independence screening and sparsifying operator (SISSO) model, to identify the best low-dimensional descriptors that guide SAA catalyst design for industrially relevant reactions. They aimed at predicting H binding energies (BE_H), H_2 dissociation energy barriers (E_b), dopant segregation energies (SE), and dopant segregation energies in the presence of adsorbed hydrogen (SE_H). DFT datasets contain more than three hundred SAAs calculated with the revised Perdew–Burke–Ernzerhof (RPBE) functional.[118] Standard correlations in computational catalyst design based on d-band center theory[67,119] and BEP relationship unfortunately fail for H adsorption on SAAs, emphasizing the need for new descriptors and SAA design principles. Instead, the SISSO model shows good predictive accuracy and was used to perform the high-throughput screening of 5000 SAA catalysts for hydrogen dissociation reactions through predicting BE_H, E_b, and SE_H. An activity descriptor incorporating E_b and the free energy of H adsorption (ΔG) as $\sqrt{\Delta G^2 + E_b{}^2}$ was developed to build a correlation between SAA reactivity and stability, and then, over 200 SAA candidates with high activity and stability were identified (Fig. 10). Overall, this study provides a robust, generalizable, and accelerated approach for evaluating SAA stability and activity.

Sun *et al.*[79] developed a ML framework to discover SAA catalysts for the chemistry of methane activation through learning the DFT-computed reaction barriers of C–H cleavage and screening a large chemical space of 10 950 SAA surfaces. They first constructed 623 DFT energy barrier data points of the first and last steps of methane dehydrogenation to train an ML regression model. Then, the ML regression model was used to screen 10 950 SAA surfaces. Feature importance analysis suggests that a descriptor related to surface energy is the dominant one (Fig. 11), which is consistent with the above findings.[63,76] This ML workflow identified two highly active and selective SAA catalysts for methane cracking, Ir/Ni(111) and Re/Ni(111). Subsequent experimental work confirms high H_2 yield rates and reasonable methane conversion rates for both ML-predicted SAAs. This study demonstrates the efficiency and robustness of the data-driven ML model in accelerating SAA catalyst design and discovering experimentally viable catalysts for methane activation. A detailed ML workflow is covered in another work (Fig. 11d).[80]

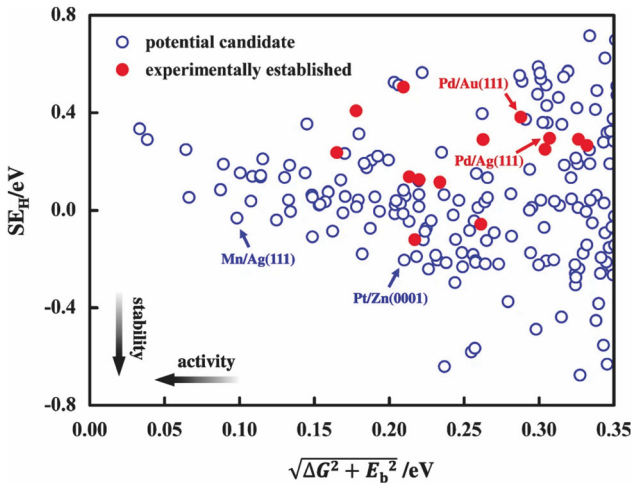

Fig. 10 Correlation between the stability and activity of experimentally established SAAs (red filled circles) and SISSO-predicted SAAs (blue empty circles). The *y*-axis represents the stability descriptor, SE_H, while the *x*-axis represents the activity descriptor, $\sqrt{\Delta G^2 + E_b[\mathrm{STAG}]^2}$. Reproduced from ref. 78, with permission from Springer Nature, copyright 2021.

A very recent work by Feng *et al.*[64] combined DFT calculations with supervised ML to discover efficient SAA catalysts for alkane dehydrogenation. They first constructed 92 DFT-calculated methane C–H activation barriers across 23 SAA surfaces and performed feature selection to narrow down 23 features to 12 optimal features for training ML models. Bagging regression (BAR) model achieved the best accuracy of an RMSE value of 0.06 eV and was then used to screen 53 SAA candidates. Feature importance analysis indicates that the dehydrogenation step index (1–4, where 1 denotes the first dehydrogenation step), surface energy, and dopant lattice constant are dominant descriptors. The significant contribution of surface energy aligns well with the above studies, confirming its critical role in governing SAA activity.[63,76,79] ML predictions identified Ru/Cu(111) as a highly active catalyst for alkane dehydrogenation. DFT calculations confirm that Ru/Cu(111) is not only active for methane dehydrogenation, but also shows high reactivity for ethane, propane, and isobutane dehydrogenation. Microkinetic modeling further reveals that Ru/Cu(111) shows a high selectivity toward generating propylene from propane dehydrogenation. Overall, this work shows an effective ML and DFT framework to guide SAA design for alkane dehydrogenation and identifies Ru/Cu(111) as a highly active and selective catalyst for C_1–C_4 activation.

Collectively, the above studies introduce the framework of applying ML models to the discovery of SAA catalysts for methane activation. An early work[76] established that simple regression models using elemental features reproduce methane dehydrogenation intermediate adsorption energies, laying the groundwork for data-driven high-throughput screening. Subsequent works[77,78] combined ML models with physics-informed principles to evaluate the catalytic performances of a vast chemical space of SAA catalysts, even extending methane dehydrogenation to other alkanes. Beyond ML model development, feature analyses consistently inform two key descriptors, *i.e.*, the periodic group and surface energy of dopant elements, in governing SAA reactivity. To summarize, ML has become an emergent tool in accelerating SAA catalyst discovery, which enables the efficient exploration of structural and compositional spaces and eventually guides experimental efforts.

Meanwhile, ML models for SAA discovery exhibit distinct trade-offs in terms of dataset size, computational efficiency, and transferability. Tree-based regression models, such as ETR

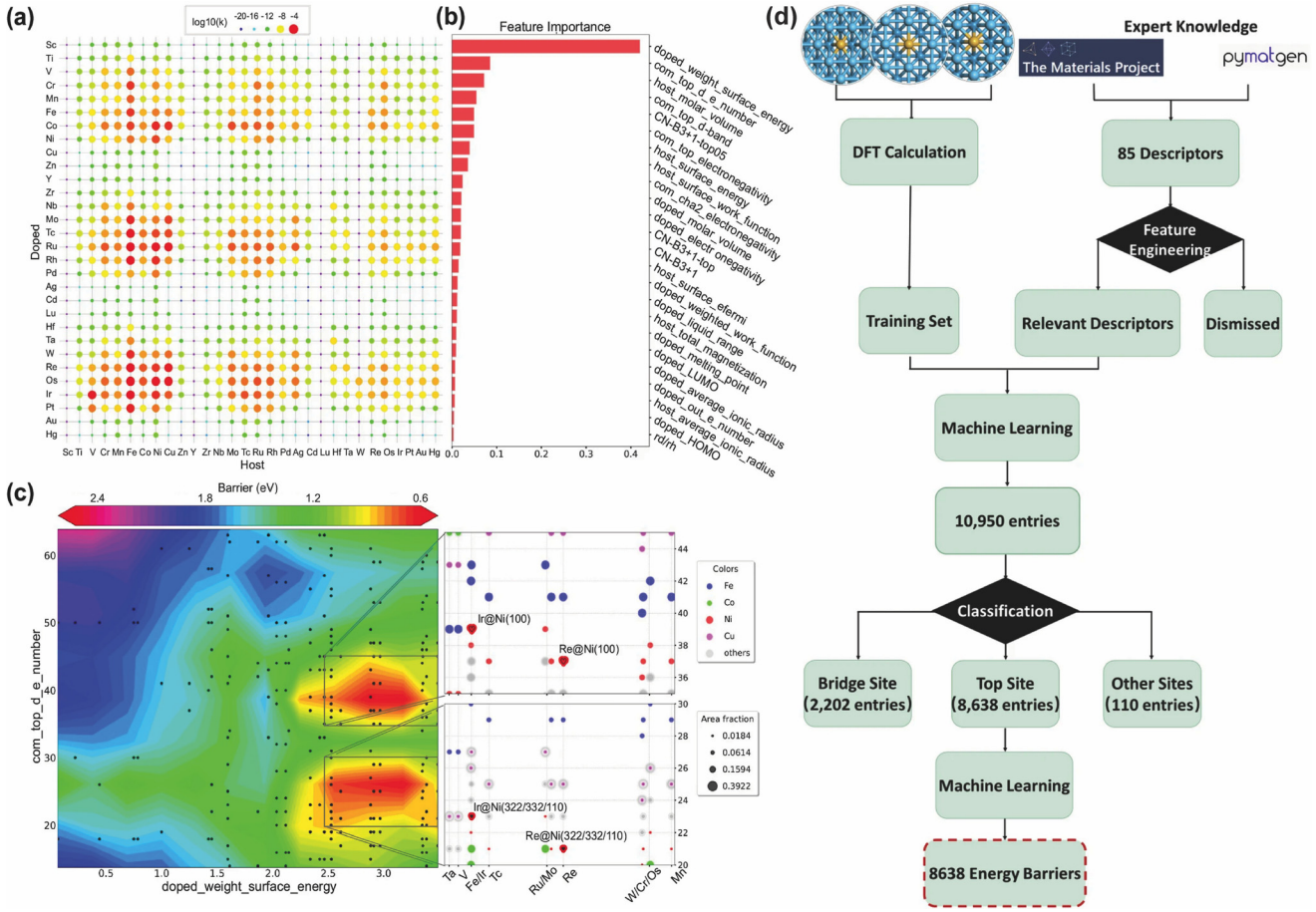

Fig. 11 (a) C–H cleavage rates of all SAA surfaces at 450 °C. (b) Feature importance analysis of 24 descriptors revealed from the ML model. (c) Two-dimensional volcano plot illustrating the relationship between the C–H dissociation barrier and the top two descriptors of screened SAA surfaces. (d) Workflow of generating C–H cleavage barrier database on SAA surfaces, including performing DFT calculations, conducting feature engineering, developing ML models, and estimating energy barriers using ML models. (a)–(c) Reproduced from ref. 79, with permission from Springer Nature, copyright 2024. (d) Reproduced from ref. 80, with permission from Springer Nature, copyright 2025.

and GBR, are highly efficient for predicting quantities, such as adsorption energies, and can be trained on relatively small datasets (in the order of ~100 DFT datapoints). Their negligible computational cost makes them attractive for rapid screening. However, they offer limited transferability and are generally less reliable when extrapolating beyond the training domain. In contrast, the SISSO approach typically relies on large datasets, often comprising hundreds of DFT datapoints, but delivers explicit, low-dimensional, and interpretable descriptors. These descriptors help uncover the underlying physicochemical factors governing catalyst stability and activity, thereby providing transferable design principles for SAA catalysts. Supervised models enable the large-scale ranking of thousands of candidate SAAs based on predicted activation barriers, although their reliability depends on rigorous out-of-sample validation and targeted DFT re-evaluations to ensure robustness and transferability. More recently, machine learning interatomic potentials (MLIPs) have emerged as the most data-intensive approach, often requiring thousands of DFT datapoints for training. Despite this high cost, MLIPs make it possible to perform finite-temperature MD simulations and capture surface dynamics under experimentally relevant conditions.

4. Computational efforts in SAAs for activating other alkanes

Beyond the chemistry of methane activation, researchers have applied both DFT calculations and ML models to understand the reactivity of SAA catalysts for activating other alkanes, such as ethane and propane. In this section, we summarize recent efforts of exploring SAA catalysts for the dehydrogenation of alkanes other than methane, where additional C–H bond breaking and reaction intermediates introduce mechanistic complexity.[27,29,61,62,65,120,121] Zhang *et al.*[65] systematically screened SAAs with Co, Ir, Ni, Pd, and Pt dopants embedded in the surface layers of Cu, Ag, and Au host metals for ethane dehydrogenation. DFT and microkinetic modeling reveal that the reactivity of ethane dehydrogenation to ethylene correlates

with (1) $*C_2H_4$ desorption energy, where an easier desorption leads to a lower activity, and (2) $*C_2H_5$ adsorption energy, where a weaker adsorption leads to a higher selectivity. Across all the studied SAA surfaces, $*C_2H_4$ desorption is kinetically more favorable than further dehydrogenation and C–C bond breaking. Ten SAAs (Co/Cu, Ni/Cu, Pd/Cu, Pt/Cu, Ir/Ag, Ni/Ag, Pd/Ag, Pt/Ag, Ni/Au, and Pd/Au) favor selective ethylene formation, and Ni/Cu SAA exhibits the best activity and selectivity, outperforming pure Pd and Pt catalysts.

In addition to the dehydrogenation of C_2 hydrocarbons, computational efforts of designing SAA catalysts have been extended to C_3 chemicals. Cao *et al.*[61] studied propane dehydrogenation on a single-Pd-doped Cu_{55} nanoparticle (Pd_1/Cu_{55}), a three-Pd-doped Cu_{55} nanoparticle (Pd_3/Cu_{55}), and a pure Cu_{55} nanoparticle (Fig. 12). They found that propane binds weakly *via* physisorption on all three nanoparticles, and the first C–H activation step is the rate-limiting step, with a barrier of 1.06 eV on Pd_1/Cu_{55}, approximately 0.25 eV lower than that on a pure Cu_{55} nanocluster. *H diffusion is kinetically favorable, with a reaction barrier of 0.16 eV, leading to favorable H_2 formation. The subsequent dehydrogenation of $*C_3H_7$ to propylene has a surmountable reaction barrier of 0.6 eV, while the further C–H activation of propylene (1.16–1.43 eV) and C–C bond cleavage (2.56 eV) are kinetically unfavorable, suggesting high selectivity toward propylene formation. Introducing two additional Pd atoms only slightly lowers the initial dehydrogenation barrier but impedes *H diffusion and propylene formation, indicating that the formation of isolated active sites in SAA enables both high activity and selectivity.

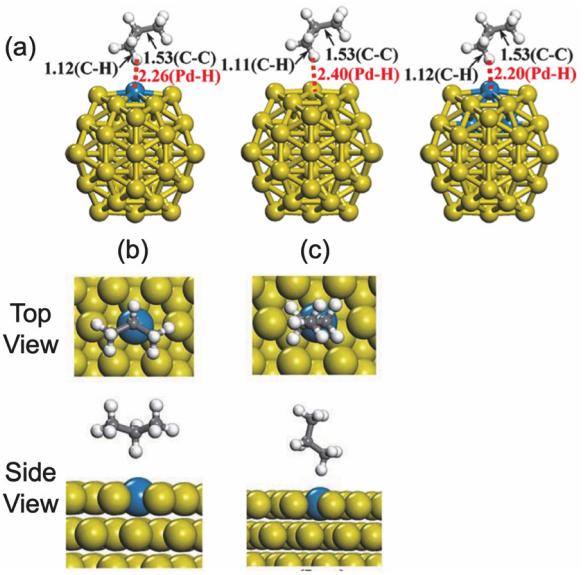

Fig. 12 (a) Optimized structures of propane adsorption on a Pd_1/Cu_{55} nanoparticle, a pure Cu_{55} nanoparticle, and a Pd_3/Cu_{55} nanoparticle. Top and side views of propane adsorption on Pd/Cu(111) with (b) parallel and (c) perpendicular configurations. (a) Reproduced from ref. 61, with permission from the American Chemical Society, copyright 2014. (b and c) Reproduced from ref. 120 with permission from the Royal Society of Chemistry, copyright 2016.

AIMD further shows that the Pd_1/Cu_{55} nanoparticle is thermodynamically stable at a temperature of 500 K. Later, the authors extended the Cu_{55} nanocluster host to an extended Cu (111) surface, forming a Pd/Cu(111) SAA in a similar DFT work.[120] The results show a systematic d-band center upshift when increasing the number of Pd dopants, which strengthens adsorbate binding strength and reduces the first C–H activation barrier from 1.65 eV of a pure Cu(111) to 1.43 eV of Pd_1/Cu(111) and 1.13 eV of Pd_3/Cu(111). C–H activation usually occurs around the active Pd sites, and the dissociated *H migrates to adjacent Cu–Cu bridge sites to release Pd active sites and enable favorable further dehydrogenation steps. Even though multiple Pd dopants might improve the activity of the initial dehydrogenation step, they also overbind intermediates and lead to coke formation, consistent with their previous conclusions on Cu nanoclusters.[61] To summarize, the above studies demonstrate that single Pd dopants in the surface layer of Cu enhance selective C–H activation in propane to propylene. Hu and Cao[121] extended this work by integrating DFT-calculated energetics with *in silico* vibrational spectroscopy, *i.e.*, Infrared and Raman spectroscopies, to identify possible intermediates and elucidate reaction pathways on Pd/Cu(111) with parallel and perpendicular propane adsorption sites (Fig. 12). This work demonstrates the importance of using vibrational spectroscopy for investigating the reaction mechanisms of long-chain alkane dehydrogenation, in which multiple competing pathways exhibit similar adsorption configurations and energetics.

Sun *et al.*[27] focused on the same reaction of propane dehydrogenation, but on a Pt/Cu SAA. They showed that the incorporation of single Pt atoms on Cu catalysts broke the scaling relationship for propane dehydrogenation[122] due to the significantly reduced binding strength of propene. In addition, the first two C–H activation barriers on Pt/Cu SAA are similar to those on a pure Pt(111). However, further dehydrogenation is suppressed on Pt/Cu SAA with high reaction barriers of above 2 eV, which are much higher than those on pure Pt catalysts. Meanwhile, they discovered that Pt/Ag SAA exhibits similar C–H activation barriers to propane dehydrogenation, but is not stable in the form of SAA. In a separate work, Hannagan *et al.*[29] investigated Rh/Cu(111) SAA for propane dehydrogenation and found that the first C–H activation barrier could be reduced to 0.57 eV, compared to 1.39 eV on Cu(111), 0.68 eV on Pt(111), and 0.63 eV on Rh(111), highlighting its superior activity. In addition, the reaction barrier of the further dehydrogenation step to $*C_3H_6$ on Rh/Cu(111) is extremely low, *i.e.*, 0.1 eV (Fig. 13), leading to propene formation. The superior activity and selectivity of Rh/Cu(111) SAA for propane to propene conversion were experimentally confirmed in the same work.

Bunting *et al.*[62] combined DFT calculations, ML-trained interatomic potentials, and molecular dynamics (MD) simulations to perform a systematic study of the reactivity of Rh/Cu and Pd/Cu SAAs for propane dehydrogenation (Fig. 14). They first trained equivariant neural-network interatomic potentials (NequIP) using around 9000 DFT single-point calculations per

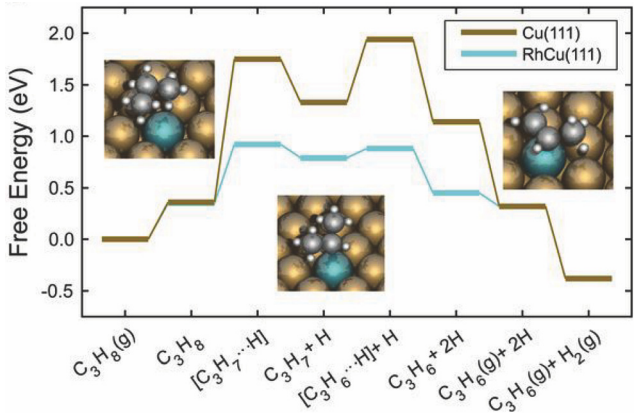

Fig. 13 Energy profile of Rh/Cu(111) SAA and Cu(111) for propane dehydrogenation to propene. Energies are referenced to the clean slabs and a gas-phase C_3H_8. H denotes a H atom adsorbed on the surfaces. Reproduced from ref. 29, with permission from AAAS, copyright 2021.

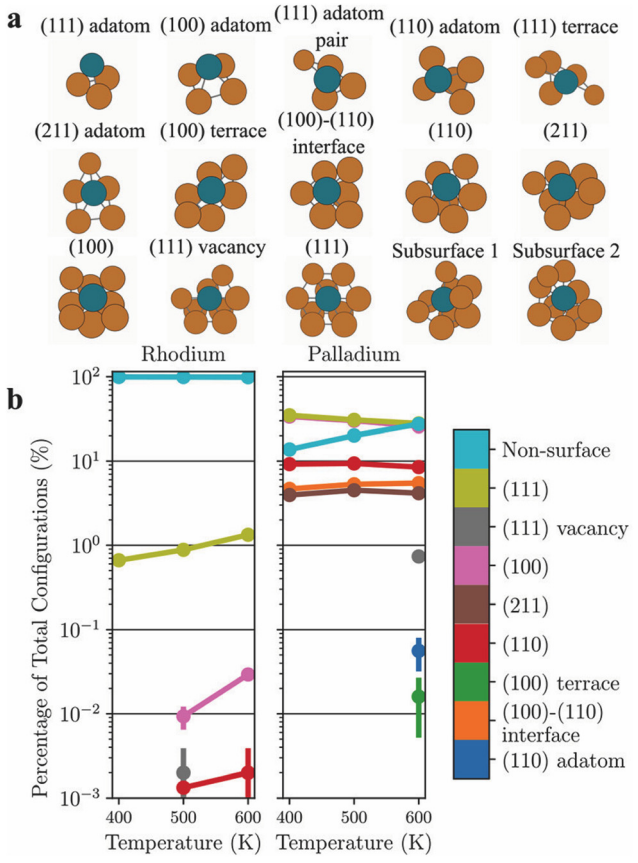

Fig. 14 (a) Representative structures of 13 possible surface and two subsurface dopant sites for Cu-based SAAs. (b) Probability of dopant occupation at each site, obtained from MD simulations and transmutation Monte Carlo simulations using the ML-trained interatomic potentials. Surface sites are color-coded according to their classification, and all non-surface sites are grouped into the non-surface category. Reproduced from ref. 62, with permission from the American Chemical Society, copyright 2023.

SAA, generated from MD trajectories and transmutation Monte Carlo swaps over a wide temperature range of 200–1200 K. These ML-trained interatomic potentials enable the large-scale MD simulations of a 3 nm Wulff-constructed Cu nanoparticle at experimentally relevant temperatures. Site-specific free energy pathways for C–H activation and propene and H_2 desorption were then proposed by combining DFT calculations and microkinetic modeling. MD simulations reveal that Rh dopants preferentially reside on the (111) facet, while Pd dopants exhibit broad distributions among multiple facets, including undercoordinated sites, which are much more reactive for C–H cleavage. For both dopants, the (111) terrace sites exhibit the lowest activity for propane dehydrogenation. Therefore, accounting for the dynamic behaviors leads to activity predictions that deviate by orders of magnitude from those simply using a static (111) facet, which typically overestimates Rh/Cu(111) activity while underestimating Pd/Cu(111) activity.

The multi-scale computational tools discussed in sections 2–4 play distinct yet complementary roles in the systematic design of SAA catalysts. DFT establishes the mechanistic foundation by identifying active sites and quantifying reaction energies and activation barriers on SAAs, thereby rationalizing the dopant–host synergy. For example, DFT studies show that isolated dopant sites can substantially reduce the first C–H activation barrier on Pt/Cu(111) relative to Cu(111), providing a microscopic explanation for enhanced low-temperature activity.[28] To bridge these static 0 K predictions with experimental conditions, AIMD captures finite-temperature effects, surface dynamics, and entropic contributions at elevated temperatures. This is illustrated by the studies of the temperature-dependent C–H activation of CHD_3 on Pt/Cu(111) SAA[53] and the thermal stability of Pd_1/Cu_{55} nanoparticles.[61] Microkinetic modeling then translates these DFT-derived energetics into macroscopic observables, such as rates and selectivity, enabling direct comparison with experimental performance. The microkinetic modeling of ethane dehydrogenation over Ni/Cu SAAs has been used to predict ethylene yields and assess selectivity trends.[65] Despite their mechanistic rigor, first-principles methods are computationally demanding and therefore limited in scalability when exploring the broad compositional and structural space. Consequently, ML emerges as a powerful strategy to address these limitations by leveraging DFT-generated datasets to enable high-throughput screening and to uncover transferable design principles across a vast chemical space. Such ML-driven approaches have successfully identified novel, experimentally viable candidates for methane activation, including Ir/Ni(111) and Re/Ni(111).[79]

5. Conclusions and outlook

This review provides a summary of recent computational progress in understanding and designing SAA catalysts for the activation of methane and other light alkanes. We first presented first-principles studies, with DFT calculations, AIMD

simulations, and microkinetic modeling, across extensive dopant–host SAA combinations. These studies revealed several mechanistic insights into methane and other alkane activation on SAA catalysts: (i) the transition states of the initial C–H cleavage were localized around the active dopant region, yielding activation barriers similar to those on the pure dopant metal; (ii) less reactive host atoms moderately bound intermediate species, suppressing further dehydrogenation and thereby avoiding coke formation; and (iii) the synergy between dopant and host metal enhanced selective C–C coupling towards multi-carbon hydrocarbons. We next summarized the accelerated SAA catalyst design work with a powerful computational tool, ML, which had transformed SAA discovery from case-by-case exploration to high-throughput screening through the accurate predictions of adsorption energies and activation barriers using interpretable descriptors. Finally, we extended the review from methane activation to the activation of multi-carbon alkanes.

Across computational studies, the most commonly adopted activity descriptor for methane activation is the reaction barrier associated with the first C–H bond cleavage. Among widely studied host metals (Cu, Ag, and Au) and dopants (Ni, Pd, Pt, and Rh), Rh-doped SAAs consistently exhibit the lowest activation barriers, with representative values of ~0.55–0.64 eV reported for Rh/Ag(111), Rh/Au(111), and Rh/Cu(111). When full dehydrogenation pathways are studied on Cu-based SAAs, Rh/Cu(111) is repeatedly identified as one of the most reactive candidates, which benefits from dopant–host synergy that mitigates excessive dehydrogenation compared with pure dopant metals. Beyond these typical SAAs, Ir-doped SAAs have been predicted to exhibit exceptionally high activity on selected facets, such as Ir/Pt(110), where a near-zero initial barrier has been reported. However, such studies often focus solely on the first C–H bond cleavage and therefore require the further evaluation of subsequent dehydrogenation steps and possible coking susceptibility. Finally, recent data-driven screening efforts have broadened the design space for methane decomposition catalysts, identifying promising systems, including Ni-based SAAs and emerging Cu-based candidates, such as Ru/Cu(111), which combine high activity with improved resistance to over-dehydrogenation.

Looking forward, numerous opportunities remain to further advance SAA catalysis. First, the accessible structural and compositional space should extend beyond the conventional paradigm of dispersing an active dopant within an inert host. The systematic exploration of underexplored dopant–host combinations, non-traditional catalytic transition metals, and stepped or defect-rich facets may reveal novel structure–composition–property relationships. To make such expansion both practical and accurate, the field should evolve from conventional high-throughput DFT screening toward active-learning workflows with uncertainty quantification. Such approaches can prioritize the most informative SAA candidates for DFT validation and thereby accelerate discovery in underexplored chemical spaces. Second, improving transferability will require the establishment of benchmark "anchor sets", *i.e.*, shared reference calculations performed on a small, agreed-upon list of SAAs and elementary steps computed using consistent settings. These anchor sets would enable cross-study normalization and more reliable comparisons of activities. Third, there is a critical need for general, physics-informed descriptors and design principles that remain robust across diverse dopants, hosts, and facets. To achieve this, advanced quantum mechanical simulations beyond standard DFT, such as embedded correlated wavefunction theory,[44–46,123–125] can enable a more rigorous description of electronic structures and thereby yield more reliable descriptors for SAA catalysis. In parallel, advanced ML frameworks with explicit uncertainty quantification can improve robustness and generalizability across different alkane chemistries. Finally, realizing these goals will benefit from collaborative data ecosystems. The development of open, standardized SAA databases and benchmarking protocols would enable the cross-validation of models and ensure that descriptors developed for methane activation remain transferable to long-chain hydrocarbon chemistry. Overall, the tight integration of the first-principles theory, data-efficient ML, and community data sharing will be essential for translating computational insights into industrially relevant, low-carbon alkane valorization using SAA catalysts.

Conflicts of interest

There are no conflicts of interest to declare.

Data availability

No primary research results, software or code have been included and no new data were generated or analyzed as part of this review.

Acknowledgements

The authors acknowledge support from the donors of the ACS Petroleum Research Fund under the Doctoral New Investigator Grant 68077-DNI5 and from the National Science Foundation under Award No. CBET-2440175.

References

1 P. Schwach, X. Pan and X. Bao, *Chem. Rev.*, 2017, **117**, 8497–8520.
2 B. Wang, S. Albarracín-Suazo, Y. Pagán-Torres and E. Nikolla, *Catal. Today*, 2017, **285**, 147–158.
3 P. Zhai, Y. Li, M. Wang, J. Liu, Z. Cao, J. Zhang, Y. Xu, X. Liu, Y.-W. Li, Q. Zhu, D. Xiao, X.-D. Wen and D. Ma, *Chem*, 2021, **7**, 3027–3051.
4 L. Sun, Y. Wang, N. Guan and L. Li, *Energy Technol.*, 2019, **8**, 1900826.

5 M. Jafarbegloo, A. Tarlani, A. W. Mesbah and S. Sahebdelfar, *Int. J. Hydrogen Energy*, 2015, **40**, 2445–2451.
6 J. O. Ighalo and P. B. Amama, *Int. J. Hydrogen Energy*, 2024, **51**, 688–700.
7 X. Guo, G. Fang, G. Li, H. Ma, H. Fan, L. Yu, C. Ma, X. Wu, D. Deng, M. Wei, D. Tan, R. Si, S. Zhang, J. Li, L. Sun, Z. Tang, X. Pan and X. Bao, *Science*, 2014, **344**, 616–619.
8 A. Blankenship, M. Artsiusheuski, V. Sushkevich and J. A. van Bokhoven, *Nat. Catal.*, 2023, **6**, 748–762.
9 C. Karakaya and R. J. Kee, *Prog. Energy Combust. Sci.*, 2016, **55**, 60–97.
10 E. Meloni, M. Martino and V. Palma, *Catalysts*, 2020, **10**, 352.
11 J. Yu, T. Le, D. Jing, E. Stavitski, N. Hunter, K. Lalit, D. Leshchev, D. E. Resasco, E. H. Sargent, B. Wang and W. Huang, *Nat. Commun.*, 2023, **14**, 7514.
12 A. A. Latimer, A. Kakekhani, A. R. Kulkarni and J. K. Nørskov, *ACS Catal.*, 2018, **8**, 6894–6907.
13 S. Ma, X. Guo, L. Zhao, S. Scott and X. Bao, *J. Energy Chem.*, 2013, **22**, 1–20.
14 C. Díaz-Urrutia and T. Ott, *Science*, 2019, **363**, 1326–1329.
15 C. Wang, Y. Xu, L. Xiong, X. Li, E. Chen, T. J. Miao, T. Zhang, Y. Lan and J. Tang, *Nat. Commun.*, 2024, **15**, 7535.
16 P. Bhumla, M. Kumar and S. Bhattacharya, *Nanoscale Adv.*, 2021, **3**, 575–583.
17 J. Kim, M. S. Abbott, D. B. Go and J. C. Hicks, *ACS Energy Lett.*, 2016, **1**, 94–99.
18 P. Tomkins, M. Ranocchiari and J. A. van Bokhoven, *Acc. Chem. Res.*, 2017, **50**, 418–425.
19 R. T. Hannagan, G. Giannakakis, M. Flytzani-Stephanopoulos and E. C. H. Sykes, *Chem. Rev.*, 2020, **120**, 12044–12088.
20 M. B. Boucher, B. Zugic, G. Cladaras, J. Kammert, M. D. Marcinkowski, T. J. Lawton, E. C. Sykes and M. Flytzani-Stephanopoulos, *Phys. Chem. Chem. Phys.*, 2013, **15**, 12187–12196.
21 X. Cao, A. Mirjalili, J. Wheeler, W. Xie and B. W. L. Jang, *Front. Chem. Sci. Eng.*, 2015, **9**, 442–449.
22 J. Liu, J. Shan, F. R. Lucci, S. Cao, E. C. H. Sykes and M. Flytzani-Stephanopoulos, *Catal. Sci. Technol.*, 2017, **7**, 4276–4284.
23 C. M. Kruppe, J. D. Krooswyk and M. Trenary, *ACS Catal.*, 2017, **7**, 8042–8049.
24 M. T. Darby, R. Réocreux, E. C. H. Sykes, A. Michaelides and M. Stamatakis, *ACS Catal.*, 2018, **8**, 5038–5050.
25 M. T. Darby, M. Stamatakis, A. Michaelides and E. C. H. Sykes, *J. Phys. Chem. Lett.*, 2018, **9**, 5636–5646.
26 S. Hasegawa, S. Takano, S. Yamazoe and T. Tsukuda, *Chem. Commun.*, 2018, **54**, 5915–5918.
27 G. Sun, Z. J. Zhao, R. Mu, S. Zha, L. Li, S. Chen, K. Zang, J. Luo, Z. Li, S. C. Purdy, A. J. Kropf, J. T. Miller, L. Zeng and J. Gong, *Nat. Commun.*, 2018, **9**, 4454.
28 M. D. Marcinkowski, M. T. Darby, J. Liu, J. M. Wimble, F. R. Lucci, S. Lee, A. Michaelides, M. Flytzani-Stephanopoulos, M. Stamatakis and E. C. H. Sykes, *Nat. Chem.*, 2018, **10**, 325–332.
29 R. T. Hannagan, G. Giannakakis, R. Réocreux, J. Schumann, J. Finzel, Y. Wang, A. Michaelides, P. Deshlahra, P. Christopher, M. Flytzani-Stephanopoulos, M. Stamatakis and E. C. H. Sykes, *Science*, 2021, **372**, 1444–1447.
30 K. Ji, M. Xu, S. M. Xu, Y. Wang, R. Ge, X. Hu, X. Sun and H. Duan, *Angew. Chem., Int. Ed.*, 2022, **61**, e202209849.
31 A. R. Poerwoprajitno, L. Gloag, J. Watt, S. Cheong, X. Tan, H. Lei, H. A. Tahini, A. Henson, B. Subhash, N. M. Bedford, B. K. Miller, P. B. O'Mara, T. M. Benedetti, D. L. Huber, W. Zhang, S. C. Smith, J. J. Gooding, W. Schuhmann and R. D. Tilley, *Nat. Catal.*, 2022, **5**, 231–237.
32 H. Yin, Y. Peng and J. Li, *Environ. Sci. Technol.*, 2023, **57**, 3134–3144.
33 S. Li, C. W. Wang, X. Zhao, J. S. Dang and J. Li, *J. Phys. Chem. Lett.*, 2024, **15**, 5088–5095.
34 M. Kothakonda, S. LaCroix, C. Zhou, J. Yang, J. Su and Q. Zhao, *ACS Catal.*, 2025, **15**, 11608–11616.
35 C. Zhou, M. Kothakonda and Q. Zhao, *J. Catal.*, 2025, **448**, 116194.
36 R. Reocreux, P. L. Kress, R. T. Hannagan, V. Cinar, M. Stamatakis and E. C. H. Sykes, *J. Phys. Chem. Lett.*, 2020, **11**, 8751–8757.
37 X. Liu, X. Wang, S. Zhen, G. Sun, C. Pei, Z. J. Zhao and J. Gong, *Chem. Sci.*, 2022, **13**, 9537–9543.
38 Y. Xing, L. Kang, J. Ma, Q. Jiang, Y. Su, S. Zhang, X. Xu, L. Li, A. Wang, Z.-P. Liu, S. Ma, X. Y. Liu and T. Zhang, *Chin. J. Catal.*, 2023, **48**, 164–174.
39 J. Lin, M. Shen, C. Zhang, S. Bi, G. Shen, F. Gao and W. Li, *Chem. Eng. J.*, 2025, **519**, 165243.
40 G. Sun, R. Luo, D. Fu, K. Wu, X. Wang, X. Bian, Z. Lu, X. Chang, Z. Wang, S. Huang, Y. Zhu, J. Zhou, S. Chen, C. Pei, Z. J. Zhao and J. Gong, *Science*, 2025, **390**, eadw3053.
41 Y. Chang, M. Jia, B. Niu, M. Xie and C. Zhou, *Energy Fuels*, 2019, **33**, 9289–9301.
42 C. Zhou, Y. Chang, P. Wang, B. Niu and M. Jia, *Energy Fuels*, 2020, **34**, 16654–16665.
43 C. Zhou, D. Liu and A. Farooq, *Combust. Flame*, 2024, **261**, 113289.
44 Q. Zhao, J. M. P. Martirez and E. A. Carter, *J. Am. Chem. Soc.*, 2021, **143**, 6152–6164.
45 Q. Zhao, J. M. P. Martirez and E. A. Carter, *Proc. Natl. Acad. Sci. U. S. A.*, 2022, **119**, e2202931119.
46 Q. Zhao, J. M. P. Martirez and E. A. Carter, *J. Phys. Chem. Lett.*, 2022, **13**, 10282–10290.
47 C. Gallagher, W. Siddiqui, T. Arnold, C. Cheng, E. Su and Q. Zhao, *J. Phys. Chem. C*, 2024, **128**, 2876–2883.
48 C. Gallagher, M. Kothakonda and Q. Zhao, *Phys. Chem. Chem. Phys.*, 2025, **27**, 5464–5475.
49 C. Zhou and Q. Zhao, *ChemPhysChem*, 2025, **26**, e202401097.
50 A. Kokalj, N. Bonini, S. De Gironcoli, C. Sbraccia, G. Fratesi and S. Baroni, *J. Am. Chem. Soc.*, 2006, **128**, 12448–12454.

51 Y. Zhao, S. Li and Y. Sun, *J. Catal.*, 2013, **34**, 911–922.
52 R. Zhang, T. Duan, L. Ling and B. Wang, *Appl. Surf. Sci.*, 2015, **341**, 100–108.
53 N. Gerrits, D. Migliorini and G. J. Kroes, *J. Chem. Phys.*, 2018, **149**, 224701.
54 Z. Jiang, Z. Wu, T. Fang and C. Yi, *Chem. Phys. Lett.*, 2019, **715**, 323–329.
55 H. Khettal, M. F. Haroun and M. Boukelkoul, *Comput. Theor. Chem.*, 2020, **1186**, 112890.
56 A. Akça, *Open Phys.*, 2020, **18**, 790–798.
57 Y. Ren, X. Liu, Z. Zhang and X. Shen, *Phys. Chem. Chem. Phys.*, 2021, **23**, 15564–15573.
58 W. Zhou, Y. Chen, L. Tan, Q. Tang, C. Lu and L. Dong, *AIChE J.*, 2023, **69**, e18118.
59 L. Zhou, Y.-Q. Su and T.-L. Hu, *Sci. China Mater.*, 2023, **66**, 3189–3199.
60 N. Dong, T. Roman and C. Stampfl, *Catalysts*, 2024, **14**, 145.
61 X. Cao, Y. Ji and Y. Luo, *J. Phys. Chem. C*, 2014, **119**, 1016–1023.
62 R. J. Bunting, F. Wodaczek, T. Torabi and B. Cheng, *J. Am. Chem. Soc.*, 2023, **145**, 14894–14902.
63 S. Saxena, T. S. Khan, F. Jalid, M. Ramteke and M. A. Haider, *J. Mater. Chem. A*, 2020, **8**, 107–123.
64 H. Feng, Z. Ge, Y. Deng, P. Pu, S. Zhao, X. Song, H. Yuan, Y. Wu, J. Yang, Y. Si, A. Politano, X. Zhang and Y.-W. Zhang, *J. Catal.*, 2025, **448**, 116213.
65 Y. Zhang, B. Wang, M. Fan, D. Li and R. Zhang, *Fuel*, 2021, **306**, 121641.
66 M. Neurock, *J. Catal.*, 2003, **216**, 73–88.
67 J. K. Nørskov, T. Bligaard, J. Rossmeisl and C. H. Christensen, *Nat. Chem.*, 2009, **1**, 37–46.
68 M. M. Montemore and J. W. Medlin, *Catal. Sci. Technol.*, 2014, **4**, 3748–3761.
69 J. Greeley, *Annu. Rev. Chem. Biomol. Eng.*, 2016, **7**, 605–635.
70 A. J. Medford, A. Vojvodic, J. S. Hummelshøj, J. Voss, F. Abild-Pedersen, F. Studt, T. Bligaard, A. Nilsson and J. K. Nørskov, *J. Catal.*, 2015, **328**, 36–42.
71 H. A. Doan, C. Li, L. Ward, M. Zhou, L. A. Curtiss and R. S. Assary, *Digital Discovery*, 2023, **2**, 59–68.
72 L. H. Mou, T. Han, P. E. S. Smith, E. Sharman and J. Jiang, *Adv. Sci.*, 2023, **10**, 2301020.
73 P. Pisal, O. Krejčí and P. Rinke, *npj Comput. Mater.*, 2025, **11**, 213.
74 X. Jia, T. Wang, D. Zhang, X. Wang, H. Liu, L. Zhang and H. Li, *J. Catal.*, 2025, **447**, 116162.
75 C. Ren, Y. Cui, Q. Li, C. Ling and J. Wang, *J. Am. Chem. Soc.*, 2025, **147**, 13610–13617.
76 T. Toyao, K. Suzuki, S. Kikuchi, S. Takakusagi, K.-i. Shimizu and I. Takigawa, *J. Phys. Chem. C*, 2018, **122**, 8315–8326.
77 K. K. Rao, Q. K. Do, K. Pham, D. Maiti and L. C. Grabow, *Top. Catal.*, 2020, **63**, 728–741.
78 Z. K. Han, D. Sarker, R. Ouyang, A. Mazheika, Y. Gao and S. V. Levchenko, *Nat. Commun.*, 2021, **12**, 1833.
79 J. Sun, R. Tu, Y. Xu, H. Yang, T. Yu, D. Zhai, X. Ci and W. Deng, *Nat. Commun.*, 2024, **15**, 6036.
80 H. Wang, J. Sun, Y. Li and W. Deng, *Sci. Data*, 2025, **12**, 648.
81 H. Xin, T. Mou, H. S. Pillai, S.-H. Wang and Y. Huang, *Acc. Mater. Res.*, 2023, **5**, 22–34.
82 J. P. Perdew, K. Burke and M. Ernzerhof, *Phys. Rev. Lett.*, 1996, **77**, 3865–3868.
83 J. P. Perdew and Y. Wang, *Phys. Rev. B: Condens. Matter Mater. Phys.*, 1992, **45**, 13244–13249.
84 M. Dion, H. Rydberg, E. Schroder, D. C. Langreth and B. I. Lundqvist, *Phys. Rev. Lett.*, 2004, **92**, 246401.
85 J. Klimes, D. R. Bowler and A. Michaelides, *J. Phys.: Condens. Matter*, 2010, **22**, 022201.
86 J. Klimeš, D. R. Bowler and A. Michaelides, *Phys. Rev. B: Condens. Matter Mater. Phys.*, 2011, **83**, 195131.
87 J. Klimes and A. Michaelides, *J. Chem. Phys.*, 2012, **137**, 120901.
88 G.-J. Kroes, *Phys. Chem. Chem. Phys.*, 2021, **23**, 8962–9048.
89 S. S. Yadavalli, G. Jones and M. Stamatakis, *Phys. Chem. Chem. Phys.*, 2021, **23**, 15601–15612.
90 K. Omata, *Ind. Eng. Chem. Res.*, 2011, **50**, 10948–10954.
91 Y. Saad, D. Gao, T. Ngo, S. Bobbitt, J. R. Chelikowsky and W. Andreoni, *Phys. Rev. B: Condens. Matter Mater. Phys.*, 2012, **85**, 104104.
92 K. Hansen, G. Montavon, F. Biegler, S. Fazli, M. Rupp, M. Scheffler, O. A. von Lilienfeld, A. Tkatchenko and K. R. Muller, *J. Chem. Theory Comput.*, 2013, **9**, 3404–3419.
93 A. A. Emery, J. E. Saal, S. Kirklin, V. I. Hegde and C. Wolverton, *Chem. Mater.*, 2016, **28**, 5621–5634.
94 R. Gomez-Bombarelli, J. Aguilera-Iparraguirre, T. D. Hirzel, D. Duvenaud, D. Maclaurin, M. A. Blood-Forsythe, H. S. Chae, M. Einzinger, D. G. Ha, T. Wu, G. Markopoulos, S. Jeon, H. Kang, H. Miyazaki, M. Numata, S. Kim, W. Huang, S. I. Hong, M. Baldo, R. P. Adams and A. Aspuru-Guzik, *Nat. Mater.*, 2016, **15**, 1120–1127.
95 A. Khorshidi and A. A. Peterson, *Comput. Phys. Commun.*, 2016, **207**, 310–324.
96 G. Pilania, A. Mannodi-Kanakkithodi, B. P. Uberuaga, R. Ramprasad, J. E. Gubernatis and T. Lookman, *Sci. Rep.*, 2016, **6**, 19375.
97 Z. W. Ulissi, A. R. Singh, C. Tsai and J. K. Nørskov, *J. Phys. Chem. Lett.*, 2016, **7**, 3931–3935.
98 L. Ward, A. Agrawal, A. Choudhary and C. Wolverton, *npj Comput. Mater.*, 2016, **2**, 1–7.
99 H. Altae-Tran, B. Ramsundar, A. S. Pappu and V. Pande, *ACS Cent. Sci.*, 2017, **3**, 283–293.
100 B. Kolb, L. C. Lentz and A. M. Kolpak, *Sci. Rep.*, 2017, **7**, 1192.
101 A. A. Peterson, R. Christensen and A. Khorshidi, *Phys. Chem. Chem. Phys.*, 2017, **19**, 10978–10985.
102 A. W. Thornton, C. M. Simon, J. Kim, O. Kwon, K. S. Deeg, K. Konstas, S. J. Pas, M. R. Hill, D. A. Winkler, M. Haranczyk and B. Smit, *Chem. Mater.*, 2017, **29**, 2844–2854.

103 E. J. Ras, M. J. Louwerse, M. C. Mittelmeijer-Hazeleger and G. Rothenberg, *Phys. Chem. Chem. Phys.*, 2013, **15**, 4436–4443.
104 E.-J. Ras and G. Rothenberg, *RSC Adv.*, 2014, **4**, 5963–5974.
105 T. Bligaard, R. M. Bullock, C. T. Campbell, J. G. Chen, B. C. Gates, R. J. Gorte, C. W. Jones, W. D. Jones, J. R. Kitchin and S. L. Scott, *ACS Catal.*, 2016, **6**, 2590–2602.
106 A. Comas-Vives, K. Larmier and C. Coperet, *Chem. Commun.*, 2017, **53**, 4296–4303.
107 F. Göltl, P. Müller, P. Uchupalanun, P. Sautet and I. Hermans, *Chem. Mater.*, 2017, **29**, 6434–6444.
108 R. Jinnouchi and R. Asahi, *J. Phys. Chem. Lett.*, 2017, **8**, 4279–4283.
109 Z. Li, X. Ma and H. Xin, *Catal. Today*, 2017, **280**, 232–238.
110 Z. Li, S. Wang, W. S. Chin, L. E. Achenie and H. Xin, *J. Mater. Chem. A*, 2017, **5**, 24131–24138.
111 A. L. Allred and E. G. Rochow, *J. Inorg. Nucl. Chem.*, 1958, **5**, 264–268.
112 A. L. Allred and E. G. Rochow, *J. Inorg. Nucl. Chem.*, 1958, **5**, 269–288.
113 W. M. Haynes, *CRC Handbook of Chemistry and Physics*, CRC Press, Boca Raton, FL, 2016.
114 R. Tran, Z. Xu, B. Radhakrishnan, D. Winston, W. Sun, K. A. Persson and S. P. Ong, *Sci. Data*, 2016, **3**, 160080.
115 H. Zhuang, A. J. Tkalych and E. A. Carter, *J. Phys. Chem. C*, 2016, **120**, 23698–23706.
116 X. Li, R. Chiong and A. J. Page, *J. Phys. Chem. Lett.*, 2021, **12**, 5156–5162.
117 B. Hammer and J. K. Nørskov, *Adv. Catal.*, 2000, **45**, 71–129.
118 B. Hammer, L. B. Hansen and J. K. Nørskov, *Phys. Rev. B: Condens. Matter Mater. Phys.*, 1999, **59**, 7413–7421.
119 A. Ruban, B. Hammer, P. Stoltze, H. L. Skriver and J. K. Nørskov, *J. Mol. Catal. A: Chem.*, 1997, **115**, 421–429.
120 X. Cao, *RSC Adv.*, 2016, **6**, 65524–65532.
121 W. Hu and X. Cao, *Molecules*, 2018, **23**, 126.
122 A. Khorshidi, J. Violet, J. Hashemi and A. A. Peterson, *Nat. Catal.*, 2018, **1**, 263–268.
123 F. Libisch, C. Huang and E. A. Carter, *Acc. Chem. Res.*, 2014, **47**, 2768–2775.
124 Q. Zhao and E. A. Carter, *J. Chem. Theory Comput.*, 2020, **16**, 6528–6538.
125 Q. Zhao, X. Zhang, J. M. P. Martirez and E. A. Carter, *J. Chem. Theory Comput.*, 2020, **16**, 7078–7088.